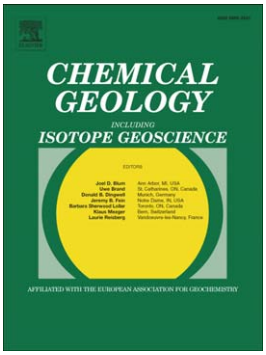

A fresh approach to investigating CO_2 storage: Experimental CO_2-water-rock interactions in a low-salinity reservoir system

S.M. Farquhar, J.K. Pearce, G.K.W. Dawson, A. Golab, S. Sommacal, D. Kirste, D. Biddle, S.D. Golding

PII: S0009-2541(14)00445-8
DOI: doi: 10.1016/j.chemgeo.2014.10.006
Reference: CHEMGE 17370

To appear in: *Chemical Geology*

Accepted date: 2 October 2014

Please cite this article as: Farquhar, S.M., Pearce, J.K., Dawson, G.K.W., Golab, A., Sommacal, S., Kirste, D., Biddle, D., Golding, S.D., A fresh approach to investigating CO_2 storage: Experimental CO_2-water-rock interactions in a low-salinity reservoir system, *Chemical Geology* (2014), doi: 10.1016/j.chemgeo.2014.10.006

A fresh approach to investigating CO_2 storage: Experimental CO_2-water-rock interactions in a low-salinity reservoir system

S.M. Farquhar[1], J.K. Pearce[1,2], G.K.W. Dawson[1], A. Golab[3], S. Sommacal[3], D. Kirste[2,4], D. Biddle[5] and S.D. Golding[1]*

[1]*School of Earth Sciences, University of Queensland, QLD 4072, Australia*

[2]*Cooperative Research Centre for Greenhouse Gas Technologies, Canberra, ACT 2601, Australia*

[3]*Lithicon Australia, Canberra, ACT, 2600, Australia*

[4]*Department of Earth Sciences, Simon Fraser University, Burnaby, BC, Canada*

[5]*School of Chemical Engineering, University of Queensland, QLD 4072, Australia*

**susan.farquhar@uqconnect.edu.au*

Abstract

The interactions between CO_2, water and rock in low-salinity host formations remain largely unexplored for conditions relevant to CO_2 injection and storage. Core samples and sub-plugs from five Jurassic-aged Surat Basin sandstones and siltstones of varying mineralogy have been experimentally reacted in low-salinity water with supercritical CO_2 at simulated in situ reservoir conditions (P = 12 MPa and T = 60 °C) for 16 days (384 h), with a view to characterising potential CO_2-water-rock interactions in fresh or low-salinity potential siliclastic CO_2 storage targets located in Queensland, Australia. CO_2-water-rock reactions were coupled with detailed mineral and porosity characterisation, obtained prior to and following reaction, to identify changes in the mineralogy and porosity of selected reservoir and seal rocks during simulated CO_2 injection. Aqueous element concentrations were measured from fluid extracts obtained periodically throughout the experiments to infer fluid-rock reactions over time. Fluid analyses show an evolution of dissolved concentration over time, with most major (e.g. Ca, Fe, Si, Mg, Mn) and minor (e.g. S, Sr, Ba, Zn) components increasing in concentration during reaction with CO_2. Similar trends between elements reflect shared sources and/or similar release mechanisms, such as dissolution and desorption with decreasing pH. Small decreases in concentration of selected elements were observed towards the end of some experiments; however, no precipitation of minerals was directly observed in petrography. Sample characterisation

on a fine scale allowed direct scrutiny of mineralogical and porosity changes by comparing pre- and post-reaction observations. Scanning electron microscopy and registered 3D images from micro-computed tomography (micro-CT) indicate dissolution of minerals, including carbonates, chlorite, biotite members, and, to a lesser extent, feldspars. Quantitative mineral mapping of sub-plugs identified dissolution of calcite from carbonate cemented core, with a decrease in calcite content from 17 vol. % to 15 vol. % following reaction, and a subsequent increase in porosity of 1.1 vol. %. Kinetic geochemical modelling of the CO_2-water-rock experiments successfully reproduced the general trends observed in aqueous geochemistry for the investigated major elements. After coupling experimental geochemistry with detailed sample characterisation and numerical modelling, expected initial reactions in the near-well region include partial dissolution and desorption of calcite, mixed carbonates, chloritic clays and annite due to pH decrease, followed in the longer-term by dissolution of additional silicates, such as feldspars. Dissolution of carbonates is predicted to improve injectivity in the near-well environment and contribute to the eventual re-precipitation of carbonates in the far field.

Keywords:

CO_2 storage

Low-salinity reservoirs

Surat Basin

CO_2-water-rock interactions

Batch reaction experiments

Micro-CT

1. INTRODUCTION

Geological storage of carbon dioxide is one of the mitigation strategies currently being investigated to reduce CO_2 emissions from source nodes, with similar processes involving supercritical CO_2 injection occurring routinely in the petroleum industry through enhanced oil recovery (EOR) (Bachu et al., 1994). Current investigations of potential CO_2 storage solutions identify aquifers as particularly attractive, in part due to their extensive potential storage capacities, favourable poro-permeability characteristics, and their geographical proximity to CO_2 source nodes (Bachu et al., 1994; Michael et al., 2009). To date, investigations into CO_2-water-rock interactions have largely focussed on CO_2 storage in deep saline aquifers for the purpose of atmospheric CO_2 mitigation. Previous experimental investigations in particular have focussed extensively on simulating the interaction between CO_2, water and rock in formation water with a saline composition, commonly in the range of 1–3 M NaCl (e.g. Rosenbauer et al., 2005; Bertier et al., 2006; Wigand et al., 2008; Ketzer et al., 2009; Luquot et al., 2012; Wilke et al., 2012; Yu et al., 2012).

By contrast, aquifer reservoir systems that have the necessary potential storage capacity and that are geographically desirable for CO_2 storage in Queensland, Australia, generally have low salinity; this necessitates further investigation of CO_2-water- rock interactions in freshwater formation conditions (Bradshaw et al., 2009; Hodgkinson and Grigorescu, 2012; Farquhar et al., 2013). Previous work on CO_2-water-rock interactions in freshwater formations has been limited. To date, the limited studies involving fresh groundwater compositions have largely focussed on the potential risk of CO_2 leakage into freshwater bodies following CO_2 injection into underlying targeted saline formations (Nicot, 2008; Birkholzer et al., 2009; Smyth et al., 2009), rather than studying low-salinity aquifers as reservoirs in their own right. Additionally, previous experimental work simulating water-CO_2-rock interactions has predominantly been conducted with disaggregated material (Little and Jackson, 2010; Lu et al., 2010; Humez et al., 2013) or with single or pure mineral samples (Wilke et al., 2012), rather than attempting to untangle the complications that arise from using naturally variable whole rock samples. Similarly, many studies use elevated temperature conditions to accelerate reactions with a view to predicting the long-term effects of CO_2 injection (Gunter et al., 1997; Kaszuba et al., 2003;

Ketzer et al., 2009), or to accommodate regions with high geothermal gradients (Kaszuba et al., 2005). However, this may actually lead to thermodynamically inaccessible reactions occurring. Short-term batch reaction experiments using mineralogically-variable samples help shed light on the complex interactions of storage systems, and can be used as a basis to predict and understand the long-term response of CO_2-water-rock interactions in natural aquifer systems (Wilke et al., 2012).

As a result, the interactions between a targeted Australian freshwater aquifer system and supercritical CO_2 in fresh water were investigated at simulated in situ reservoir conditions by measuring the extract reaction fluids over time, and observing changes to the reactant rock samples. This study aimed to observe and characterise the chemical response of a targeted fresh to low-salinity aquifer system to CO_2 injection by experimentally reacting core samples from five Jurassic-aged Surat Basin sandstones and siltstones of differing lithologies with freshwater and supercritical CO_2 at simulated in situ reservoir conditions (P = 12 MPa and T = 60 °C) for 16 days (~384 h). Unlike many previous studies, this study will include detailed characterisation of core samples prior to and following reaction with CO_2 to aid kinetic geochemical modelling and experimental interpretations of CO_2-water-rock interactions.

2. CARBON DIOXIDE STORAGE AND GEOCHEMICAL INTERACTIONS

2.1 CO_2 storage processes

Long-term storage of CO_2 can occur through various potential trapping mechanisms, including stratigraphic or structural containment, dissolution and long-term migration of CO_2-saturated formation water, residual CO_2 trapping in pore spaces, and the precipitation of carbonate minerals (Gunter et al., 1993; Bachu et al., 1994).

The physical trapping mechanisms employed in CO_2 injection and storage practices are largely analogous to those found in conventional hydrocarbon accumulation traps. Buoyant immiscible or free-phase fluids are contained by a regional low-permeability seal (Bachu and Bennion, 2008; Hovorka et al., 2009) and collected in structural or stratigraphic traps created due to the geometry of the reservoir, as discussed initially in the context of hydrocarbons (Biddle and Wielchowsky, 1994),

and in the context of CO_2 storage in detail by several authors (e.g. Benson and Cook, 2006; Bachu et al., 2007; Solomon et al., 2008; Bradshaw et al., 2009; Holloway, 2009, among others). Examples of structural and stratigraphic traps include anticlines, changes in lithofacies or reductions in permeability due to secondary alteration, unconformities and faults.

Hydrodynamic trapping, which involves long CO_2 residence times resulting from low hydraulic gradients, employs both physical and chemical trapping mechanisms. These mechanisms occur in the form of residual trapping of the CO_2 plume tail in pore spaces and localised matrix heterogeneities (Solomon et al., 2008; Bradshaw et al., 2009; Holloway, 2009), and as solubility trapping, where CO_2 dissolves and becomes miscible in water and then migrates through diffusion, dispersion and convection with the aquifer's regional hydrodynamic regime (Koide et al., 1992; Bachu et al., 1994; Benson and Cook, 2006; Bachu et al., 2007; Assayag et al., 2009). Finally, CO_2-water-rock reactions can lead to mineral trapping, where CO_2 is permanently contained through carbonate mineralisation, with divalent cation bearing silicalistic reservoirs having the highest sequestration potential (Gunter et al., 1993; Bachu et al., 1994; Gunter et al., 1997).

2.2 Implications of CO_2-freshwater-rock interactions

During injection, CO_2 dissolves in formation waters to form aqueous CO_2 and carbonic acid, this drives down the pH leading to a disequlibrium between formation water and minerals, resulting in chemical reactions. The solubility of CO_2 in water is dependent on the pressure-temperature (P-T) conditions and ionic strength, with aqueous CO_2 solubility generally increasing with pressure, and decreasing with temperature and salinity (Rosenbauer and Koksalan, 2002; Duan and Sun, 2003). Injecting CO_2 at high pressure into lower-salinity reservoirs, as opposed to brackish or brine reservoirs, will allow more CO_2 to be dissolved into formation waters. This will also reduce bouyency-driven migration of the CO_2 plume due to smaller density differences between the CO_2 plume and formation waters, which would lead to longer CO_2 residence times in line with low-velocity migration of formation waters (Bachu, 2000). An added potential benefit of CO_2 injection in fresh or low-salinity reservoirs could involve the enhancement of poro-permeability in the near-well environment during injection from material dissolution.

2.2.1 Implications of chemical interactions on reservoir quality

The implications of CO_2-water-rock interactions, summarised below, are reviewed by Gaus (2011) in the context of brine aquifers, but are also largely applicable to low-salinity reservoirs. During dissolution of CO_2 in water, the weak acid H_2CO_3 forms and dissociates in the water (1):

$$CO_2 + H_2O \leftrightarrow H_2CO_3 \leftrightarrow H^+ + HCO_3^- \quad \textbf{1.}$$

This results in a decrease in pH, which in turn induces dissolution of minerals of the host rock and may result in desorption of ions from mineral surfaces (Apps et al., 2010). Interactions involving reactive minerals, for example carbonates, will result in buffering of the pH and a reduction in acidity (2):

$$\underset{\text{calcite}}{CaCO_3} + H^+ \leftrightarrow Ca^{2+} + \underset{\text{bicarbonate}}{HCO_3^-} \quad \textbf{2.}$$

The dissolution of minerals can extend to the silicates, as well as carbonates, with examples for albite (3 and 4) and Fe-rich chlorite (5), adapted from Gunter et al. (1997), Watson (2006) and Gaus (2010):

$$\underset{\text{albite}}{NaAlSi_3O_8} + CO_{2(aq)} + H_2O \leftrightarrow \underset{\text{dawsonite}}{NaAlCO_3(OH)_2} + \underset{\text{silica}}{3SiO_2} \quad \textbf{3.}$$

$$\underset{\text{albite}}{7NaAlSi_3O_8} + 6CO_{2(aq)} + 6H_2O \leftrightarrow \underset{\text{bicarbonate}}{6HCO_3^-} + 6Na^+ + \underset{\text{silica}}{\text{Na-smectite}} + 10SiO_2 \quad \textbf{4.}$$

$$\underset{\text{Fe-chlorite}}{Fe_4Mn_1Al_2Si_3O_{10}(OH)_8} + \underset{\text{calcite}}{5CaCO_3} + 5CO_{2(aq)}$$

$$\leftrightarrow \underset{\text{ankerite}}{5Ca(Fe_{0.8}Mn_{0.2})(CO_3)_2} + \underset{\text{kaolinite}}{Al_2Si_2O_5(OH)_4} + \underset{\text{silica}}{SiO_2} + H_2O \quad \textbf{5.}$$

These CO_2-water-rock interactions have considerable implications in the near-well environment, in terms of porosity and permeability changes, as a result of dissolution and precipitation, but are not well studied for low-salinity environments.

Field and experimental applications of CO_2 injection have shown that dissolution of minerals may occur at the dissolved CO_2 front, increasing porosity and permeability (Gunter et al., 1997; Kaszuba et al., 2005), whilst physical mobilisation of non-reactive minerals and precipitation of minerals can substantially reduce porosity and permeability (Gibson-Poole et al., 2005; Civan, 2007; Kaldi and Gibson-Poole, 2008). During CO_2 injection, these processes could be either beneficial or deleterious, depending on the location in a reservoir system. Although an increase in permeability due to

dissolution of minerals in sealing units would be unwanted, an increase in permeability in the reservoir close to the wellbore could potentially allow an increase in CO_2 flow rate, and lead to a lower pressure-gradient in the near-well environment (Gunter et al., 1993). In addition, whilst precipitation of secondary minerals may reduce permeability in a reservoir unit, precipitation of silicate or carbonate minerals may lead to the sealing of fractures, or reductions in porosity and permeability in overlying caprocks (Rosenbauer et al., 2005; Shukla et al., 2010).

3. METHODOLOGY

3.1 Geological setting and hydrogeological characteristics

Whole-rock core samples were obtained from three Early to Middle Jurassic Surat Basin formations, which comprise a targeted storage system in Queensland, Australia (Farquhar et al., 2013). Reactant samples were selected to represent different lithologies commonly found in siliclastic reservoir systems, with each sample interval exhibiting different mineralogy and porosity. This study focussed on three units in the Surat Basin system: the Precipice Sandstone, Evergreen Formation and Hutton Sandstone (Figure 1). This targeted reservoir system comprises a relatively clean primary reservoir (Precipice Sandstone) overlain by a variably fine-grained, low-permeability seal (Evergreen Formation) and a heterogeneous, internally baffled, secondary reservoir or seal (Hutton Sandstone). Groundwater in the Jurassic-aged clastic sequences is predominantly fresh, with a total dissolved solids (TDS) content of about 500–1500 mg/L and a pH between 7.5 and 8.5 (Cresswell et al., 2012) across the Surat Basin.

3.1.1 Precipice Sandstone

The Precipice Sandstone sample is a clean, porous, fine- to coarse-grained quartzose sandstone, with minor grain-coating and pore-filling kaolin and relict feldspars and trace detrital muscovite. Porosity reduction from pressure-solution contacts is observed; however, porosity has been greatly enhanced by feldspar dissolution, and potentially through the extensive dissolution of previous diagenetic cements (Farquhar et al., 2013).

The hydrochemistry of the Precipice Sandstone is predominantly very fresh (TDS ≤ 1500 mg/L) and Na—HCO_3 type in the Surat Basin. These values are biased towards sampling of the shallower intervals of the units, and may not be representative of the deeper intervals (Hodginkson et al., 2009). Porosity in the Precipice Sandstone has been previously reported as 16 ± 5 %, with a mean horizontal permeability of 320 ± 905 mD. Permeability is much higher (500–1000 mD) in the Mimosa Syncline, within which the study area of interest lies (Kellett et al., 2012).

3.1.2 Evergreen Formation

The Evergreen Formation is chiefly a fine- to medium-grained argillaceous wacke to quartzose sandstone, interbedded with carbonaceous mudstone and sandy siltstone. Potentially reactive minerals include the predominantly Ca-poor feldspars, clays (kaolinite, Fe-chlorite, smectite), detrital micas and varying quantities of carbonates (calcite, ankerite and siderite). Porosity is highly variable within the unit, with intervals of porous fine, quartzose sandstone towards the base of the unit, interbedded with clay-rich finer-grained intervals that have experienced significant burial compaction to effectively remove porosity, as shown by the formation of a pseudomatrix formed from ductilely-deformed fine-grained lithics. The hydrochemistry of the Evergreen Formation is more variable than that of the Precipice and Hutton sandstones, with fresh to brackish compositions reported (Hodginkson et al., 2009). The Evergreen Formation constitutes an aquitard, with lower average porosity (15 ± 6 %) and horizontal permeability (87 ± 245 mD) (Kellett et al., 2012). Permeabilities are variable, but are generally lower in the region of interest.

3.1.3 Hutton Sandstone

The Hutton Sandstone mainly consists of well-sorted, fine to medium-grained, lithic-feldspathic arenites, with finer-grained lithic-rich intervals, and coarser-grained intervals that show partial to extensive dissolution of detrital feldspars, lithics and carbonates. Potentially reactive minerals in the Hutton Sandstone include feldspars (K-rich), micas, clays (chlorite, smectite-rich) and carbonates, which comprise calcite, ankerite and siderite. Extensive diagenetic carbonate cement is observed in one of the Hutton Sandstone samples from ~799 m (Farquhar et al., 2013).

Hydrochemical signatures in the Hutton Sandstone are largely fresh or marginally brackish and Na—HCO_3 type (Hodginkson et al., 2009). The Hutton Sandstone has a higher reported mean porosity (22 ± 6 %) and horizontal permeability (426 ± 1334 mD) (Kellett et al., 2012). Permeability in the study area is highly variable, but is generally higher than in the depocentre of the Mimosa Syncline.

3.2 CO_2 batch-reaction experiment setup

The experiments were conducted in a static batch reactor (Figure 2) comprising an unstirred 250 mL Parr reactor vessel with corrosion-resistant thermoplastic (PEEK) lining and sampling assembly, equipped with an electronic heating apparatus and fitted to an automatic PC-based temperature and pressure system, described in detail in this issue by Pearce et al. (2014). Pressure was achieved using a syringe pump and measured using a pressure transducer. Temperature was maintained using an external heating jacket with feedback to the control loop, achieved with a thermocouple. Pressure and temperature measurements were logged at one-minute intervals. Maintaining temperature inside the vessel resulted in a sinusoidal variation in temperature (T = 60 ± 0.5 °C) and a corresponding minor variation in pressure (e.g. P = 120 ± 1 bar for CO_2).

A system of valved tubes allows fluids to be introduced and effluent withdrawn during the experiment. This facilitates the periodic extraction of experimental leachate through a sampling port to be measured ex situ, and also allows for the addition of gases during the experiment. At the cessation of each experiment, the vessel was slowly depressurised and allowed to cool to below ~50 °C prior to sampling of the remnant experiment fluid and retrieval of reacted rock samples.

Prior to conducting each experiment run, sample holders were acid cleaned and the batch reactor was flushed using two cycles of CO_2 flushes with deoxygenated purified water to minimise procedural contamination. Fluid chemistry of effluent from the second clean CO_2 cycle was used as a procedural blank for the subsequent experiment.

3.3 Experiment conditions for the Surat Basin

3.3.1 Pressure-temperature conditions

Experiments were conducted at simulated pressure-temperature condition at a depth of 1.2 km in the north-eastern Surat Basin, where P = 12 MPa and T = 60 °C. These conditions are taken to reflect measured down-hole temperatures in the study area; whilst a raw 71 °C bottom-hole temperature for Chinchilla 4 was recorded at 1255 m (Almond, 1985), a corrected down-hole temperature of 61 °C was reported in nearby well Rockwood-1 in the Precipice Sandstone at 1155 m depth (Raza et al., 2009).

3.3.2 Simulated formation water and gas fluid chemistry

Formation water chemistry for the Precipice Sandstone and Hutton Sandstone is generally fresh in composition, whilst highly variable fresh to brackish water compositions are reported for the Evergreen Formation (Hodginkson et al., 2009). For these experiments, a purified (filtered and deionised) water composition was adopted as the experiment solvent to simulate fresh water reservoir chemistry for all three formations, to simplify interpretation of elemental signatures, and allow direct comparison between the rock samples. Formation water compositions were constrained by equilibrating the samples with purified water during the N_2 soaking period at experimental temperature and pressure. This method provides a baseline composition to use as a comparison during CO_2 experiments by dissolving any salts, colloids, etc. in the pore fluids that could change fluid chemistry prior to CO_2 introduction. In the absence of representative in situ formation water chemistries, these N_2 baseline compositions were also used as a proxy for initial system water chemistries during kinetic modelling. Due to the use of ion-undersaturated purified water, metal release may potentially be over-predicted with respect to using in situ measured formations water compositions.

Whilst actual flue gas compositions from combustion systems like coal-fired power plants are likely to contain contaminants in addition to CO_2, including N_2, Ar, O_2 and SO_2, etc. (Wilke et al., 2012; Pearce et al., 2014), this study used pure food-grade CO_2 to simulate CO_2 captured for injection purposes. A concurrent and complimentary study in this issue by Pearce et al. (2014) investigates the

comparative effect of using impure mixed fluids (CO_2, SO_2 and water) in reactions with the same experimental conditions.

3.3.3 Experiment procedure

A summary of the stages of the CO_2-water-rock experiments, including the cleaning and sampling procedure for the batch reactions, is shown in Table 1.

Prior to commencing the CO_2-reaction stage of the experiments, whole-rock core samples were fully submerged in purified water (70 mL) and exposed to supercritical N_2 for ~24 h at 60 °C and 12 MPa to allow a baseline fluid or background water composition to be determined. In a similar low-salinity study conducted at near-atmospheric, low-temperature conditions (20 °C and 2 bar) by Humez et al. (2013), the authors used pH as an indicator of equilibration between samples and fluid during a N_2, pre-CO_2 phase. The authors found that pH plateaued after a very short time (15 mins), and commenced introduction of CO_2 after 260 min, indicating little need for a prolonged equilibration stage. Following the 24-hr N_2 soak, supercritical CO_2 was introduced into the reactor to flush the N_2 and return the vessel to full pressure (12 MPa). A flushing period was applied prior to each stage of pressurising the vessels with the respective fluid (supercritical N_2 or CO_2) to remove oxygen from the system.

The experiment was allowed to react for 16 days (~384 h) with the introduced supercritical CO_2. Incremental fluid samples were extracted periodically over the 16 days, with additional CO_2 injected when needed to recover minimal pressure drops. Extract ports and lines were also flushed with CO_2 prior to and following sampling, to minimise contamination between samples. Two aliquots were collected per sample, with 1.5–5 mL collected per sample. One aliquot was taken for ex situ measurement of pH, conductivity and temperature—obtained directly after extraction, when cooled to ~30 °C—using a TPS WP81 pH meter and electrode previously calibrated to buffer solutions (pH 4.07, 7.00 and 9.00) at 25 °C, with an error of ± 0.01. The second aliquot was acidified with a 1–2 % spike using 70 % HNO_3 for chemical analysis by ICP-OES with a Perkins Elmer 8300 D.V. instrument. Selected non-acidified samples were reserved for anions analysis for alkalinity by potentiometric titration (± 0.01 mg/kg), chloride ion concentration (± 0.01 mg/kg) by ferricyanide

discrete analysis (CAS no. 16887-00-6), and sulphate concentration (± 0.01 mg/kg) by UV-VIS Spectrophotometry (CAS no. 14808-79-8) at ALS Environmental Division, Brisbane.

3.4 Reactant sample selection

Five rock samples from the potential reservoir system were selected for reaction based on mineralogical and petrographic studies. These five samples are taken to be representative of the different lithologies and geochemistries found within the target reservoir system. One sample was selected from the relatively homogeneous potential primary reservoir (Precipice Sandstone), and two samples each were taken from the more complex primary seal unit (Evergreen Formation) and secondary seal and/or reservoir unit (Hutton Sandstone).

Two experiment runs were conducted for each of the five rock samples (Table 2); a whole cube (15 mm × 15 mm × 15 mm), cylindrical plug (3–8 mm × 5–7 mm), plus an offcut of variable dimensions was used for one experiment run ("Run A"), and a single half-cube (15 mm × 15 mm × 7.5 mm) was used for an additional experiment run ("Run B"). The fluid-to-rock ratio for each run is approximately 7:1 (Run A) and 23:1 (Run B), with 70 mL purified (filtered and deionised) water used in reactions. One of the experiment runs (run A) for one sample (Evergreen Formation, 1138 m) was conducted in 100 mL of 1 % KCl solution to preserve sample integrity and allow post-reaction imaging, as the brother sample from the prior experiment run (run B) had disintegrated during reaction with purified water. The calcite-cemented sub-plug (Hutton 799 m) was wrapped in Mylar heatshrink to preserve sample integrity during CO_2 reaction and allow post-reaction imaging.

4. ANALYTICAL TECHNIQUES

4.1 Sample characterisation and fluid chemistry

Mineral composition of the reactant samples was determined using X-ray diffraction (XRD) at The University of Queensland (UQ). Helium, or skeletal, grain density was measured for samples prior to and post experimentation using an AccuPyc II 1340 Pycnometer. High pressure mercury injection capillary pressure (MICP) tests were performed on the unreacted and reacted offcut core samples

using a PoreSizer 9320, with an associated resolution of <0.1μL and an accuracy of ±1 % of the maximum penetrometer volume. Whole-rock major-oxide chemistry was determined by inductively coupled plasma optical emission spectrometry (ICP-OES) analysis using lithium metaborate digestion, including loss on ignition (LOI). Detection limits (3σ) for major oxides are 0.001 wt% for total Fe_2O_3, K_2O, MnO, Na_2O and SiO_2; 0.002 wt% for Al_2O_3, CaO, MgO and TiO_2; and 0.003 wt% for P_2O_5.

Element abundances for the fluid extract samples were analysed using a Perkins Elmer 8300 D.V. ICP-OES at UQ. Pre- and post-reaction images of the reactant cubes were obtained by scanning electron microscopy (SEM) fitted with energy-dispersive X-ray spectrometry (EDS), using a JEOL6460 instrument at UQ, as described in detail in Dawson et al. (this issue). Auxiliary mineral analyses were performed by electron microprobe at The Australian School of Petroleum, Adelaide University, to determine specific mineral chemistries. Standardization with international standards was performed, and standard deviations were <0.5 % for major elements and <3 % for trace elements. X-ray micro-computed tomography (HeliScan micro-CT) was undertaken by Lithicon Australia, Canberra.

4.2 Micro-CT and QEMSCAN

3D micro-computed tomography (micro-CT) can be used to non-destructively image solid objects at the micron scale using X-rays (Carlson et al., 2003). Tomograms, comprising pixels (2D) or voxels (3D), portray the relative attenuation of X-rays through the sample, with voids seen in black, Al-bearing minerals in grey, and Fe-rich minerals in bright grey, reflecting increasing X-ray opacity (Golab et al., 2012). This technique allows detailed 3D characterisation and quantification of the distribution of X-ray distinct minerals, e.g. framework grains and matrix clay, and inter- and intra-granular porosity within a sample plug (e.g. Figure 3a,b). Pore structure and interconnectivity can be derived from the 3D map of pore space (Golab et al., 2010), to give static and dynamic properties. Prior to reaction, small cylindrical plugs (sub-plugs) of the rock samples were imaged in 3D at the micron scale by micro-CT. An end was trimmed off from each plug and a polished section prepared

for higher-resolution 2D SEM imaging, followed by automated quantified SEM-EDS mineral mapping (QEMSCAN). The remainder of the sub-plug was then reacted in the batch reactor at simulated basin conditions, before being re-imaged in 3D by micro-CT. After reaction, another polished section of the sub-plug was prepared for SEM and QEMSCAN mineral mapping. The 3D tomograms were then registered in perfect geometric alignment with the 2D SEM images (Figure 3c,d), which are obtained from a polished cross-sectional slice of the plug. These nm-scale SEM images are capable of evaluating submicron features such as pore-filling clay material with microporosity, acting as an internal calibration tool for the 3D porosity calculation (Knackstedt et al., 2013). The 3D tomogram and 2D SEM images were then registered to the 2D mineral map from QEMSCAN (Figure 3d,e), allowing 3D quantification of mineralogy (Golab et al., 2013). Finally, the pre- and post-reaction tomograms were registered to each other in order to map the changes caused by CO_2-water-rock interactions in 3D.

4.3 Geochemical modelling

Mineral reactions can be chemically modelled using kinetic rate equations to predict dissolution and precipitation processes that may occur in a solution over time. The reaction rate equation adopted (6) is a function of mineral reactive surface area, a reaction-rate constant specific to the mineral, a factor to account for inhibiting or catalysing species, and finally the closeness to saturation, with a chemical affinity factor to account for decreased reaction rates on approach to equilibrium.

$$r_k = A_S k_+ \prod_j (a_j)^{P_j} \left[1 - \frac{Q}{K}\right], \qquad \textbf{6.}$$

where

r_k = reaction rate

A_s = mineral surface area

k_+ = rate constant

a_j = activity of the catalysing or inhibiting species

P_j = power for species j

Q = activity product

K = equilibrium constant

Rate constant data are generally reported at 25 °C and must be recalculated at higher temperatures using 7.

$$\log k_{+} = \log k_{25} - \frac{E_a}{2.3026R}\left[\frac{1}{T} - \frac{1}{298.15}\right], \quad \textbf{7.}$$

where

E_a = activation energy

R = molar gas constant

Mineral-dissolution rates are also dependent on pH, which is incorporated using additional rate constants and activation energies based on acidic, neutral and basic mechanisms using the mineral-specific reaction rate scripts (8). Complete details are given in the complimentary study by Pearce et al. (2014).

$$k = k_{25}^{nu}\left[\frac{-E_a^{nu}}{R}\left(\frac{1}{T} - \frac{1}{T_0}\right)\right] + k_{25}^{H}\left[\frac{-E_a^{H}}{R}\left(\frac{1}{T} - \frac{1}{T_0}\right)\right] a_H^{n_H} + k_{25}^{OH}\left[\frac{-E_a^{OH}}{R}\left(\frac{1}{T} - \frac{1}{T_0}\right)\right] a_H^{n_{OH}} \quad \textbf{8.}$$

where

E_a = apparent activation energy

R = molar gas constant

T_0 = reference temperature (298.15 K)

T = temperature (in K)

nu = neutral mechanism

H = acid mechanism

OH = base mechanism

a = activity of the catalysing species

n = power term.

Reactive surface areas were initially assigned using grain-size constraints estimated from SEM-EDS and micro-CT, and are detailed in Table 3. Mineral reactive surface areas were varied for each sample to achieve a best-fit simulation of measured experiment fluid chemistry. In particular, reactive surface areas for carbonates, chlorite, annite and phlogopite were adjusted to account for sample grain size, or to account for the variations in surface area resulting from factors such as grain coatings, grain contacts and morphology (Pearce et al., 2014).

Mineral precipitation rates are based on 9, as detailed in Pearce et al. (2014).

$$r_P = A_S k_P \left(\frac{Q}{K} - 1\right)^2 - k_N \exp\left\{\boxed{?} - \Gamma\left(\frac{1}{(T)^{\frac{3}{2}} \ln\left(\frac{Q}{K}\right)}\right)^2\right\} \quad \textbf{9.}$$

where

k_P = precipitation rate constant

k_N = nucleation rate constant (1 mol/s)

Γ = pre-exponential factor for nucleation

Geochemical modelling was undertaken in the Spec 8 and React modules using the Geochemist's Workbench 9 software package (Bethke and Yeakel, 2013), with a modified EQ3/EQ6 thermodynamic database (Delany and Lundeen, 1989), with further details given in Pearce et al. (2014). Geochemical reaction modelling requires the use of well-defined stoichiometric mineral phases. Thermodynamic data for Fe-rich chlorite (Fe_3:Mg_1) and ordered ankerite ($Ca_1Fe_{0.7}Mg_{0.3}$) were calculated using methods of Holland et al. (1998) and Davidson (1994), and for siderite data using an ideal-mixing model ($Fe_{0.9}Mg_{0.1}$) composition. Rate equations and parameters that were used in kinetic calculations are summarised in Table 3. Carbon dioxide fugacity (1.1189 mol/kg) was calculated based on the Duan and Sun (2003) solubility model for the simulated Surat Basin conditions of 60 °C, 120 bar and 0.001 mol/kg NaCl, to represent a low-salinity water composition.

Initial system water compositions were based on a combination of fluid chemistry obtained from the N_2-equilibration period (Table 1).

5. RESULTS AND DISCUSSION

5.1 Reactant sample characterisation

5.1.1 Bulk-rock sample composition

Major-oxide chemistry of the selected Jurassic Surat Basin samples is presented for each sample in Table 4, with the maximum 2σ uncertainty calculated from duplicate samples.

Major-oxide chemistry (Table 4) of the Surat Basin samples show a silica-dominated (97.9 wt% SiO_2) composition for one sample (Precipice Sandstone, 1192 m), with minor contributions from Al_2O_3, and to a lesser extent Na_2O, and Fe_2O_3, and trace amounts of P_2O_5. Evergreen Formation samples (1138 m and 897 m) have the lowest SiO_2 content and have higher levels of Al_2O_3, MgO, Na_2O and K_2O ± TiO_2, P_2O_5 and Fe_2O_3 than the other samples. The Hutton Sandstone samples are quite silica-rich

(82 wt%), and have variable levels of other components (Al_2O_3, Fe_2O_3, MgO , MnO, etc.). The lower Hutton Sandstone sample (867 m) has the highest Fe_2O_3 of the experiment samples (3.9 wt%). The calcite-cemented upper Hutton Sandstone sample (799 m) recorded significantly higher levels of CaO, and also had high LOI (8.4 wt%), consistent with the major presence of carbonate. One of the Evergreen Formation samples also had high LOI (7.2 wt%), which reflects a high organic matter content.

5.1.2 Geochemical classification

The maturity of sandstones is reflected in the SiO_2/Al_2O_3 index, with high ratios recorded for mineralogically mature (quartzose, rounded) samples, and low ratios recorded for chemically immature samples (Potter, 1978). Furthermore, Pettijohn et al. (1987) and Herron (1988) have shown that the Na_2O/K_2O and Fe_2O_2/K_2O ratios can be used to assist in determining chemical maturity and mineral stability, respectively. By extrapolation, samples with a low SiO_2/Al_2O_3 ratio and a higher Fe_2O_3/K_2O ratio should be mineralogically less stable and more prone to reactivity during supercritical CO_2 exposure. Using these classifications, the brother samples to Hutton 799 m and Hutton 867 m both plot as sublitharenites and litharenites, respectively (Figure 4a,b). Evergreen 897 m plots geochemically as a greywacke (Figure 4a) or a shale (b), while Evergreen 1138 m plots as an arkose or a wacke. Interestingly, in the Pettijohn et al. (1987) classification (Figure 4a), the Precipice Sandstone 1192 m sample has a Na_2O/K_2O ratio >5, so plots off-field and closest to the subarkose/sublitharenite border. The classification system by Herron (1988) correctly identifies the sample as a quartz arenite. The third axis from the Herron (1988) scheme, not shown in Figure 4b, classifies samples by Ca content by dividing samples into non-calcareous (Ca < 4 %), calcareous (4 % < Ca < 15 %), and carbonate (Ca > 15 %) samples. From this, only Hutton 799 m would be correctly classified as calcareous, with the remaining samples non-calcareous.

5.1.3 Micro-CT sample characterisation

Pore-scale imaging of the five sub-plugs by micro-CT with segmentation of X-ray distinct components allowed the characterisation of µm-scale features, including the 3D occurrence and distribution of heavy minerals, pores, fractures, cements, clay material and organic material. A volumetric assessment of X-ray distinct components (e.g. framework grains, porosity, heavy minerals,

etc.) is provided in Table 5 for each of the sub-plugs prior to reaction; however, fine-grained pore-filling materials with sub-resolution porosity (pores smaller than 1 voxel in size) do not allow the unambiguous assignment of mineral and porosity phases using X-ray attenuation. Instead, these micropores are grouped with the associated clay material, weathered grains and/or diagenetic cements that make up the matrix material (Knackstedt et al., 2013).

5.1.4 QEMSCAN mineral characterisation

Modal mineralogy was investigated using QEMSCAN technology, prior to reaction with supercritical CO_2, of polished sections of core sub-plugs (Figure 5, Table 6). The automated petrographic system comprises an SEM integrated with multiple light-element X-ray detectors and pulse processor technology. Back-scattered electrons (BSE) and energy dispersive (EDS) X-ray spectra are used to create digital mineral and textural maps (Golab et al., 2010). For samples with high clay content, the interaction between the electron beam and the sample surface extends ~5 µm into the rock sample. As a result, for very fine-grained material, the energy dispersive X-ray spectra collected for a given pixel may be a complex mix of multiple minerals, resulting in elemental concentrations that are "unclassified", as they cannot be matched to a known mineral phase.

Overall, a good correlation is seen between the whole-rock oxide chemistry (Table 4) and the sub-plug mineralogy determined by QEMSCAN (Table 6). For example, in general, the silica-dominated (80–98 wt% SiO_2) bulk-rock samples contain more quartz (57–98 %) than the silica-poor samples (35–38 %). Similarly, high Al_2O_3 (15–17 wt%) correlated with high kaolinite content (12–19 %) in the QEMSCAN mineral assays of the sub-plugs, and high Fe_2O_3 (3–4 wt%) content generally corresponded with higher assays of Fe-bearing mineral (e.g. chlorite, biotite-group minerals, Fe-oxides). In addition, the calcite-cemented Hutton Sandstone 799 sample recorded both high CaO in the whole-rock geochemistry (10 wt%) and high calcite content (14.6 %) in the QEMSCAN.

5.1.5 Chemical composition of selected minerals

Selected minerals from the rock samples were analysed by electron microprobe to determine chemical compositions (Table 7).

5.2 Fluid geochemistry

Incremental fluid samples obtained during batch reaction of rock samples with purified water and supercritical CO_2 at 12 MPa and 60 °C were measured for pH and fluid composition to infer CO_2-water-rock interactions using changes in analyte concentrations. Effluent fluids were measured by ICP-OES during both the A and B experiment runs.

5.2.1 pH evolution

Fluids extracted prior to the addition of rock samples generally have lower pH (~4) than those extracted following the addition of the sample and N_2 (6–6.5), and following the re-introduction of CO_2 (4–6.6) after time t = 0 (Figure 6). Due to expected partial CO_2 degassing during effluent extraction and pH measurement, reported values represent pH maxima and are not representative of in situ experiment fluid pH. The introduction of the rock sample during the N_2 soak rapidly buffered pH to ~6.5 for all samples, which is the also initial pH of the purified water used in the experiments. Generally, following the introduction of CO_2 in the experiment, the pH of most water samples initially dropped, before increasing with time. Samples from the carbonate-rich interval, Hutton 799 m, buffered the effluent samples to the highest pH maxima during the CO_2 reaction stage (6–7). The pH of water samples from reactions with quartzose rock samples (e.g. Precipice 1192 m) does not appear to recover beyond a maximum of pH ~5 during CO_2 exposure, indicating experiment fluids were not buffered as effectively as with the carbonate-rich samples.

5.2.2 Measured chemical behaviour during reaction with CO_2 and water

Although reliable in situ water chemistries in the study area have not been produced, our N_2-equilibrated water chemistries are generally consistent with the general basin chemistry values for each formation reported by Hodginkson et al. (2009), with the exception that Na and Mg are generally an order of magnitude lower in our experiments (see supplementary material tables A and B for complete A- and B-run fluid chemistry). Following CO_2-water-rock reaction but prior to depressurisation (t = 16 days), the majority of measured major, minor and trace elements showed an overall increase in concentration over time with respect to initial N_2 baseline (t = 0) conditions (Table 1) during both experimental runs, indicating element mobilisation from dissolution or desorption of material into the fluid phase. An initial rapid increase in concentration is observed for some elements during exposure to supercritical CO_2, suggesting an initial period of rapid dissolution and/or

desorption of material during this time (Figure 7). Rapid increases in the early stages of the experiment suggest fast release mechanisms, such as desorption, ion exchange on mineral surfaces, or exhaustive dissolution of finite amounts of trace minerals or very fine-grained minerals (Trautz et al., 2013). Rapid increases in cations in the early stages of the experiment may be partly attributed to acid-induced dissolution of colloidal metal hydroxides or fine clay particles when CO_2 is introduced into the system. Similarly, as aliquot samples are acidified prior to chemical analysis, the dissolution of these metal colloids or fine clay particles due to sampling acidification may mean measured trace metal concentrations are elevated in comparison to experiment waters (Lico et al., 1982). Subsequent plateauing in concentrations of elements in some samples is taken to represent the experiment fluids reaching an analyte-saturated state. However, plateauing of elements could also occur as the result of exhaustive reaction of minerals present in trace amounts, which would result in the same behaviour if completely dissolved within the first few days of exposure to CO_2. Small decreases in concentration observed for some major and minor elements may suggest the initial onset of mineral precipitation in some samples; however, this was not directly observed in optical petrography.

Figure 7 shows the evolution of selected major and selected minor elements over the duration of the A- and B-run experiments. Similar behaviour was observed during the A and B experiment runs for each sample, with the A-run experiments generally having higher concentrations of elements in solution, likely reflecting the increased initial rock mass and higher total exposed surface area of run A.

Major to minor elements that were largely preferentially mobilised during reaction of samples with supercritical CO_2 and water were Ca, Fe, Na and Si, and to a lesser extent also Mn, Mg, Sr, K, S ± Al. Relative measured dissolved ion concentrations were generally higher in the Hutton Sandstone and Evergreen Formation samples than in the Precipice Sandstone sample, with the Precipice sample mobilising considerably less dissolved Ca, Fe, K, Mg, Mn and Si. For the Hutton Sandstone samples, significantly higher concentrations of Ca, Mn and S are observed in Hutton 799 m fluid samples in comparison to the lower Hutton Sandstone (867 m). In comparison, Hutton 867 m shows elevated Al, K, Fe, Mg and Si at cessation of the experiment.

Following reaction with supercritical CO_2 and water at 12 MPa and 60 °C, trends in the relative increase in concentration over time are observed for analysed major and minor elements and trace to minor elements (Figure 7), indicating potential dissolution or desorption of minerals to increase dissolved ion concentrations with decreasing pH. Several elements exhibit similar trends in changing concentrations, potentially indicating similar mineral sources or processes. Three general trends are identified: type I behaviour shows an initial rapid increase in concentration over the first 1–2 days of reaction, prior to plateauing in a more gradual increase to slight decline. A marked example of this behaviour is seen for Ca, Mn, Sr and S (Figure 8) during the A and B runs of Hutton Sandstone 799 m. Type II trends exhibit a more linear concentration increase, and are exemplified in Figure 9 in the behaviour of Si (a), Fe (b), Mg (c) and Co (g) for most samples. Finally, elements that remain stable or decrease from their baseline concentrations constitute type III behaviour, as seen in for Na, K ± Al for the majority of samples (Figure 9d,e,f). These trends are similar to those observed in low-salinity batch experiments conducted at near-atmospheric pressure (e.g. Smyth et al., 2009; Lu et al., 2010; Humez et al., 2013). The low-pressure studies also identified similar evolutions in element concentrations, with a rapid increase in concentration with subsequent stabilisation identified as type I (Smyth et al., 2009; Lu et al., 2010; Humez et al., 2013), and little to no variation following CO_2 exposure as type III (Humez et al., 2013). In contrast, the existing low-pressure studies defined type II elements as showing a decrease in concentration to lower than pre-CO_2 levels (either with or without an initial increase), rather than the linear increase observed in this study.

5.2.3 Hutton Sandstone 799 m

Hutton 799 m recorded significant levels of Ca (up to 600 mg/kg in Run A) released into experiment fluids at the end of the experiment, 2–3 times as much as the nearest fluid sample. The rapid increase in Ca^{2+} content measured in Hutton 799 m reaction fluids during the first two days of CO_2 exposure is associated with the fast dissolution of minerals, in particular carbonates, during the early stages of the experiment (Figure 8a). This increase in Ca content is closely associated with a proportional increase in relative concentrations of Mn, Sr, and S (Figure 8b,c,d) following a type-1 dissolution trend, indicating contribution of these elements by the same carbonate source. The Ca, Fe and Mg content is predominantly attributed to the dissolution of calcite, which commonly contains Mn and Fe, with

lesser Mg (Figure 11a,c, Table 7), which is in part supported by the low increase in Si content measured in water chemistry. However, the exhaustive dissolution of trace minerals, desorption, or ion exchange with surface minerals with decreasing pH in this and other samples may also help explain the similar trends observed in some elements (e.g. between Ca, Sr, Mn, and S). Where Ca content is observed to plateau in experiment reaction fluids, buffering of pH by the dissolution and potential (re)precipitation of calcite is indicated. Scanning electron microscopy conducted pre- and post-experiment confirm extensive dissolution of carbonate in the calcite-cemented sample, to leave open porosity (Figure 11a,b).

Dissolution of cement within the sample was also observed in the difference between micro-CT 3D imaging of the sample pre- and post-exposure to CO_2 (see supplementary content video). By registering the 3D tomograms and finding the difference by subtracting the unchanged material, a 3D map of loss or gain can be derived (Figure 10). Dissolution occurred preferentially at the rock-fluid interface, at the surface of the sample, along grain faces, cleavages and on cement boundaries, to a total volumetric loss of ~2 % original calcite content.

Sulphur, observed in fluid samples in concentrations up to 12 mg/kg, also tracks the dissolution pattern of Ca, Mn, Fe, Mg and Sr, suggesting a potential magmatic component to the CO_2 accumulation source that resulted in the carbonate cement.

The comparatively low contribution of other major elements (e.g. Fe, Si, Al and K) is likely to result from a combination of the preferential dissolution and the higher proportion of carbonate in the sample when compared with other reactive minerals phases. Potential buffering of pH by carbonate dissolution after the initial rapid increase in dissolved ion concentrations could lead to higher alkalinity, which will reduce the reaction rate substantially by raising the pH.

5.2.4 Hutton Sandstone 867 m

Sampling during CO_2-water-rock experiments with sample Hutton 867 m revealed a more gradual increase in water composition components than in Hutton 799 m, and resulted in a substantially higher content of Fe and Si than from Hutton 799 m following reaction with CO_2 and water (Figure 9a,b). The high SiO_2 and Fe, in addition to the considerably lower Ca content, provide evidence for

silicate mineral dissolution being the primary source for major and minor element increases, rather than a carbonate source. Fe-chlorite, or iron-rich chloritic clays of mixed composition, comprises a major component of the sample (Figure 11d). Following reaction in these samples, Fe, Ca and Mg are identified in SEM-EDS as being leached from these clay mixtures. In the 3D micro-CT difference tomograms, obtained by subtracting pre-reaction from post-reaction 3D tomograms, this is observed through loss of X-ray absorbing material. This results in a reduction in the density of the Fe-rich chloritic material through the dissolution ± desorption of Fe, but no volumetric loss. In both SEM-EDS and micro-CT, the chloritic clays are observed to partially collapse, but not entirely dissolve (Figure 11e), suggesting preferential dissolution of Fe with the preservation of at least some of the mineral structure. Minor etching is tentatively identified on some diagenetically pre-altered K-feldspar grains (Figure 11f).

Silica is not directly observed to decrease in the chloritic-clay following leaching of Fe using semi-quantitative EDS spectra; however, this may be an artefact of apparent relative enrichment of Si following the leaching of Fe from the mineral structure. The Fe-rich mixed clays also commonly contain small proportions of Fe-rich carbonates, including Mg–Mn-bearing, Ca-poor siderite, and less commonly phosphatic or sulphurous phases that contain a spectrum of trace elements. The partial dissolution of these trace mineral phases is expected to account for at least part of the minor Co, Ni, Cr, Cu and Zn observed in the fluid chemistry. Some additional contribution to these trace metals from desorption, dissolution of colloids and/or metal exchange with mineral surfaces is also expected, but these processes are difficult to identify, and as such not directly observed in the samples. Dissolved Zn concentration, which is five-times higher than in Hutton 799 m, is likely to be attributed to sphalerite alteration.

5.2.5 Evergreen Formation 897 m

Fluid chemistry of the Evergreen Formation sample from ~897 m reveals substantial Na, Si and Fe, and minor Ca and K dissolved in reactant fluids (Figure 9). In general, the Evergreen Formation contains higher-salinity pore fluids than the other two units (Hodginkson et al., 2009), which is likely to be particularly true in finer-grained, low permeability horizons. As such, increasing Na (up to

90 mg/kg), and to a lesser extent K, could be accounted for by the mixing of Na-rich pore fluids during reaction, in addition to any potential contribution from alteration of Na-bearing mineral phases. The poor porosity and fine grainsize could slow mixed-fluid (CO_2 and water) access to the pores, resulting in an ongoing increase in Na after the N_2-equilibration stage.

Increases in Si and Fe (Figure 9a,b) are at least partly attributed to the desorption and dissolution of Fe-chloritic clay materials, as discussed for Hutton 867 m, with contributions to Fe also likely from annite, smectite and siderite, in addition to any contributions from dissolution of trace minerals or colloids. The linear, type II behaviour of Fe, Si, Mg and K all indicate progressive dissolution and/or desorption. Although Evergreen 897 m contains a higher proportion of annite and siderite than in Hutton 867 m, it contains considerably less chloritic material, so overall less Fe is dissolved in the Evergreen 897 m experiments. In particular, siderite- and chlorite-altered biotite are expected to contribute Fe when exposed to CO_2-water during reaction. Elevated Mg concentration with respect to the other samples also indicates alteration of phlogopite, chlorite and carbonates. Fresh, coarse flakes of biotite-group minerals, and even chlorite, observed in SEM appear relatively unaffected following CO_2-water reaction. For example, the coarse-grained Mg-bearing annite (Figure 12a,b), and the Fe-chlorite (Figure 12c,d) show little textural change following CO_2 exposure. In comparison, minerals that were fine-grained, or had previously been partially clay-altered prior to experimentation, generally showed more evidence of reaction (Figure 12d,e). This suggests pre-alteration may make minerals more susceptible to dissolution and further alteration during CO_2-water interactions, as noted by Beig and Lüttge (2006).

Remarkably, only a very minor Ca change (Figure 8a) is observed, on par with those of the Precipice Sandstone sample, which contains negligible carbonate and minor plagioclase feldspar.

5.2.6 Evergreen Formation 1138 m

Following CO_2-water-rock reactions at simulated Surat Basin conditions for 16 days, reaction fluids from Evergreen Formation sample 1138 m show a relatively high Ca content (Figure 8a). Interestingly, although the initial CaO content in Hutton 799 m is an order of magnitude higher than Evergreen 1138 m (10 wt.% vs. 1 wt.% respectively, Table 4), and the calcite content in the Hutton

799 m sample is considerably higher (14.6 area % vs. 0.2 area %, Table 6), this ratio was not maintained during dissolution of Ca into the fluid phase. The total dissolved Ca from the calcite-cemented sample from 799 m is less than three times that in the fine-grained 1138 m. Whilst contribution from dissolution of trace minerals or from desorption or metal exchange with clays could increase Ca content, this disparity is likely at least partly attributed to the morphology of the source minerals, as the very fine-grained minerals in the sample from 1138 m may have a comparatively larger surface area to allow proportionally more of the mineral to be reacted than the coarse-grained calcite cement in 799 m. In addition, differences in the pH of reaction fluids between the two samples could feasibly result in a difference in calcite solubility, with a higher pH from calcite buffering potentially leading to lower dissolution rates.

Si, Fe, Mg and K tend to follow a type II trend, indicating a silicate mineral source. The type I behaviour that Ca tends to follow when sourced from a carbonate is not as obvious in the sample, despite observed contribution by carbonate minerals (Figure 13). Low permeability and high compaction of the sample could result in a more linear dissolution trend of fine-grained carbonates by retarding fluid-flow, and slowing the initial rapid reactions that occur in type I trends. Remarkably, despite the fine grainsize and very low initial porosity of the sample (Figure 5e), evidence of CO_2 fluid interactions penetrating to the centre of the plug sample was observed in micro-CT, increasing the total porosity of the plug from 0.2 vol. % to 1.0 vol. % following CO_2 reaction.

5.2.7 Precipice Sandstone 1192 m

During reaction with supercritical CO_2 and purified water at simulated Surat Basin conditions, experiment water chemistries showed minor to negligible changes when compared to the other Chinchilla 4 samples (Figure 7e). The lack of element mobilisation into the reaction water is consistent with a very clean, poorly-reactive mineralogy, and very high initial quartz. The very low initial levels of Ca, Fe, Mg, Mn, K and Na containing minerals observed in SEM-EDS (Figure 14) and micro-CT are reflected in the fluid chemistry, which shows only very small amounts of these elements mobilised into reaction waters. These results are consistent with the registered digital core analysis, which reported no discernable changes to mineralogy in the Precipice 1192 m sample following

reaction with supercritical CO_2. Small increases in Fe and Si content and trace increases in Al are interpreted to reflect partial dissolution of minor phases such as Fe-rich chlorite and relict feldspars. The dissolved Al and Si observed in experiment fluid samples could be mobilised from amorphous phases such as colloidal silica and non-crystalline aluminosilicates of kaolinitic composition. Similarly, the minor to trace amounts of minerals such as smectite and/or vermiculite, and the clay alteration products of ex-feldspars and other minerals could potentially contribute to the observed Si and Al. Dissolved Cu and Zn concentrations may be derived from small reactive crystals of chalcopyrite and sphalerite, respectively, as these were observed in SEM (Figure 14a); however, the dissolution trends for these elements do not track S as would be expected if these minerals were the sole source, suggesting a minor contribution from additional sources. Carbonates were not recognised in the petrography of the sample, which is reflected in the low levels of Ca, Mn, and Mg measured in the reactant fluid.

5.3 Reacted sample characterisation

5.3.1 Measured rock properties post-reaction

Following reaction with supercritical CO_2 and purified water at simulated Surat Basin reservoir conditions for 16 days, changes in mass (*m*) of the five core rock samples were observed (Table 8). Masses of all samples decreased after reaction with purified water and CO_2, suggesting dissolution and/or removal of material during experimentation. The quartz-dominated Precipice Sandstone sample (1192 m) had the smallest mass decrease (~0.3 % of the initial CO_2-unreacted mass), with the Hutton Sandstone sample from 867 m showing a similarly small change in mass (~0.5 %). The calcite-rich Hutton Sandstone sample (799 m) recorded the greatest change in mass, with a ~3.9 % decrease in initial mass. Both Evergreen Formation samples, from 1138 m and 897 m, also recorded relative decreases (~2.4 %) in their initial recorded masses (Table 8).

Helium-derived skeletal densities (p_{He}) measured pre- and post-reaction with supercritical CO_2 and purified water are reported in Table 8. Interestingly, slight increases in skeletal or matrix density are

observed for the two Evergreen Formation samples. By contrast, the remaining samples all experienced minor decreases in helium density.

Mercury injection results of brother or sister samples taken before and after reaction with CO_2 were mixed. Initial porosity results show Precipice 1192 m to be the most porous (15.2 %), followed by Hutton 799 m (10.1 %), with the Evergreen 897 m sample having the lowest initial porosity (6.1 %). Whilst these results seem reasonable, the changes in porosity following reaction are suspect, as the calcite-cemented Hutton 799 m shows a decrease (10.1 % to 8.4 %) in porosity following reaction and Hutton 867 m shows an increase of 4 %. This seems unrealistic when considering micro-CT, SEM and fluid chemistry observations, and is likely to be an artefact of heterogeneity in sampling. The destructive nature of the technique necessitates the use of brother or sister samples, which may have substantial variations in porosity due to the heterogeneous nature of the samples.

5.3.2 Micro-CT and QEMSCAN post-reaction

Imaging by micro-CT before and after reaction with CO_2 and purified water allowed for the segmentation and 3D qualification of X-ray distinct phases in the 3D tomograms taken pre- and post-reaction. A summary of resolved mineralogy prior to and following reaction with supercritical CO_2 at simulated reservoir conditions for each sub-plug sample, as measured by QEMSCAN, is provided in Table 9. These data were obtained using QEMSCAN imaging of a 2D slice through the sub-plug, and as such are reported in area %. The polished sections from the sub-plugs pre- and post-reaction were located as close to one another as possible, down the length of the sub-plug, to minimise the impact of vertical heterogeneity. Conversely, 3D mineral and porosity components for the same sub-plugs imaged by micro-CT pre- and post-reaction with CO_2 and fresh water under simulated reservoir conditions are reported in Table 10. These data are obtained using 3D tomogram segmentation, and as such are reported in vol. %.

5.4 Numerical modelling

Kinetic geochemical modelling of sampled fluids obtained during the CO_2-water-rock experiments was conducted for the following selected aqueous major elements: SiO_2, Fe, Mg, Ca, Al, K ± Na.

Initial rock mineralogies are constrained by QEMSCAN, XRD and SEM-EDS, and are provided in Table 11. The interaction of very trace labile minerals and/or metal colloids with CO_2 and water is also expected to contribute to the observed aqueous trends; however, due to the difficulty of accurately identifying composition and quantity of materials that are below sample characterisation detection limits, these phases were excluded from kinetic modelling. Initial input water compositions were based on measured reaction fluids obtained after the N_2-soaking period, which attempted to equilibrate purified water with the rock samples to provide representative system water chemistries. Kinetic reaction modelling successfully reproduced the general trends observed in aqueous geochemistry for the investigated major elements (Figure 15).

5.4.1 Hutton Sandstone 799 m

Predicted fluid evolution for calcite-cemented Hutton Sandstone 799 m sample shows very high levels of Ca^{2+} in solution, with lesser Fe^{2+}, $SiO_2(aq)$, Mg^{2+}, and minimal K^+ and Al^{3+}. Kinetic modelling of a single dissolution phase with given mineral surface areas gave a reasonably satisfactory result (Figure 15a,b); however, an initial rapid increase is observed in the first two days of reaction, followed by a plateauing during the remainder of the experiment, which is not accounted for. This two-stage dissolution is consistent with the previously-described type I behaviour, which was reproduced in modelling by using a higher surface area (SA) for days 0–2 and a lower SA for days 2–16, with the output of the water chemistry from days 0–2 used as a starting chemistry for days 2–16. Whilst this increase in SA was artificially applied during this modelling exercise, this provides some insight into the possible release mechanisms of the system, as when the sample chemistry is modelled using a two-stage type I behaviour, the predicted chemistry successfully follows the measured experiment fluids with an even closer fit (Figure 15c,d). The indicated initial rapid dissolution could be a combination of the result of an initial rapid exposure of mineral surfaces to the CO_2 front on the subsample surface and via macroporosity, the preferential dissolution of fine-grained carbonates, and the exhaustive dissolution of easily-accessible, fine-grained material or trace mineral phases during reaction with CO_2. Limited contribution by silicate minerals is predicted, with the dissolution of calcite (Figure 16a) swamping other minerals (Figure 16b). This is also reflected in the measured

chemistry, and is observed in SEM-EDS and QEMSCAN. Interestingly, despite fluid concentrations of calcite-sourced elements (Ca, Mn, Fe) plateauing, which would indicate the fluid is reaching a saturated state with respect to these elements, kinetic modelling does not predict the precipitation of calcite over the course of the experiment, indicating that pH buffering may limit calcite reaction rates. Kinetic modelling indicates the onset of minor kaolinite precipitation towards the end of the experiment of all samples except Precipice 1192 m. The ubiquitous nature of kaolinite in all samples pre-reaction makes directly observing precipitation of kaolin in SEM a perilous task. QEMSCAN indicates an increase in kaolin content after CO_2 reaction (Table 9), suggesting the onset of kaolinite precipitation during the experiments is plausible. In Hutton 799 m, as in most samples, predicted and measured Na remained relatively unchanged throughout the experiment.

5.4.2 Hutton Sandstone 867 m

Both predicted and measured chemistry of the Hutton 867 m CO_2 reactions reveal the greatest increase in Fe and Si in experiment fluids, with lesser Ca, Mg and K, and negligible Al (Figure 15e). The contribution by Si, Fe, and Mg is largely assigned to the dissolution of Fe-rich chlorite, with minor Ca attributed to trace amounts of carbonate, largely contained within the chlorite (Figure 11d). This is seen in the predicted mineral mass changes, where leaching of Fe-chlorite is predicted to be the primary contributor to reactant fluids (Figure 16c), which is consistent with QEMSCAN (Figure 5b) and SEM-EDS observations (Figure 11e), although the contribution by dissolution of very trace minerals remains unassessed. The evolution of Si resulted in the poorest fit between predicted and measured fluid chemistry over time, with predicted SiO_2 plateauing more than measured SiO_2. This could be the result of the rate of precipitation of kaolinite being too high (Figure 16c), resulting in an unrealistic suppression of SiO_2. Alternatively, this may be the result of Si precipitating out of solution following aliquot collection, as separate samples for Si analysis were not obtained and diluted to 1:4 with DI water to preserve dissolved silica, as recommended by Lico et al. (1982). Interestingly, an increase in both kaolinite (from ~7 to ~11 area %) and quartz (from ~57 to ~59 area %) is observed in the QEMSCAN analysis of pre- and post-CO_2 polished subplug slices (Table 9).

5.4.3 Evergreen Formation 897 m

The predicted and modelled chemistry of Evergreen 897 m is very similar to that of Hutton 867 m (Figure 15e,f). Both samples have Fe-chlorite as the primary source of material undergoing dissolution during CO_2-water-rock reactions, with a corresponding increase in Fe, SiO_2 ± Mg. Analysis by SEM-EDS reveals contributions by annite and ankerite towards K, and Mg and Mn, respectively (Figure 12), which is also reflected in kinetic modelling of the reactions (Figure 16d). Supersaturation and subsequent precipitation of kaolinite is indicated to start at ~day 7 of CO_2 exposure, although this is not directly observed in SEM-EDS. A small increase in kaolin is indicated by post-reaction QEMSCAN of the plug sample (Table 9), as is an increase in K-feldspar, which is not observed in SEM-EDS or kinetic modelling. As discussed for Hutton 867 m, the imperfect fit for Si may be partly attributed to unwanted silica precipitation during sampling.

5.4.4 Evergreen Formation 1138 m

Predicted fluid chemistry of Evergreen 1138 m closely matches the measured chemistry of the CO_2-water-rock experiments (Figure 15g). Figure 16e reveals preferential dissolution of calcite, followed by ankerite, chlorite and phlogopite, as observed in SEM-EDS. Although some calcite is identified in the sample by mineral mapping, QEMSCAN failed to identify ankerite in the sample. This could be due to subsampling issues, as although every effort is made to select representative subsections, intra-sample heterogeneity makes this extremely difficult on a fine scale. Interestingly, the modal mineral assays from QEMSCAN suggest a probable decrease in area % of feldspars, in particular K-feldspar, and kaolinite (Table 9), with micro-CT (Table 10) indicating a corresponding decrease in framework grains (from 34 to 32 vol. %).

In contrast, Figure 16e depicts kaolinite precipitating from the very onset of CO_2 injection, suggesting the starting water chemistry was supersaturated with respect to kaolin.

5.4.5 Precipice Sandstone 1192 m

In order to match the experiment fluid chemistry observed, the quartzose and kaolinitic composition of the Precipice Sandstone sample necessitated the use of a mineralogy that was not directly observed by SEM-EDS or QEMSCAN (Table 11). As a result, trace amounts of ankerite, siderite and chlorite were added to the initial rock mass, in line with the expected mineralogy observed in other Precipice

samples. Using this initial composition, predicted chemistry matches the measured experimental reaction chemistry very well (Figure 15h), with linear increases in SiO_2, Fe, Ca and Mg attributed to the dissolution of trace amounts of ankerite, silica, siderite and Fe-chlorite. The contribution to SiO_2 by chalcedony is taken to represent the contribution to reactant fluids by colloidal silica, observed in other subsamples in SEM, which would have been a by-product of previous extensive alteration of feldspars during diagenesis.

5.5 Summary implications for CO_2 interactions in a freshwater reservoir system

5.5.1 Hutton Sandstone

The Lower Hutton Sandstone sample is similar in composition to the Evergreen samples, but contains less carbonate and considerably more fine-grained chlorite or mixed chlorite-smectite. Leaching of Fe from chloritic clay was observed during CO_2-water-rock reactions; however, these reactions did not lead to notable changes in poro-permeability in either SEM-EDS or digital 3D tomography, with only minor increases in clay intraporosity observed in SEM-EDS and minor reductions in X-ray dense cations in clays observed in micro-CT. This suggests that desorption from and/or dissolution of chlorite, mixed clays, or even annite or phlogopite, is unlikely to improve permeability in the formation during CO_2 injection. Furthermore, the contribution of Fe at the mixed-fluid interface could feasibly lead to siderite precipitation in the longer-term, especially in matrix heterogeneities where CO_2 becomes trapped by residual trapping.

The calcite-cemented Hutton Sandstone sample experienced considerable dissolution of the carbonate cement (from 17 vol. % to 15 vol. %) during reactions with CO_2. Dissolution is more prominent at the rock-fluid interface, with the surface of the reacted rock sample block showing extensive dissolution of cement and the surface of the plug showing preferential dissolution, with minor dissolution occurring on cleavages and at framework grain/cement boundaries. This loss of calcite cement has the potential to have considerable impact on near bore well porosity and permeability, with CO_2 injection predicted to facilitate injection by enhancing permeability and increasing pore access to mixed fluids.

Differences in the rate of dissolution may partly be related to sample grainsize and compaction, as low porosity in a compacted, fine-grained carbonate-containing sample will likely retard CO_2 fluids. This would limit exposure of reactant minerals to the CO_2-water interface, leading to a decreased rate of dissolution. In units of equal permeability, finer carbonate grainsize and a large relative surface area could result in more rapid dissolution, and proportionally more of the mineral being dissolved over time.

Although mineral precipitation was not observed or predicted beyond minor kaolinite precipitation, the substantial release of divalent cations (Ca^{2+}, Fe^{2+}, Mn^{2+}) from the dissolution of carbonates into formation waters leads to the potential for mineral trapping (10) following a drop in CO_2 fugacity (Watson, 2006).

$$Ca^{2+} + Mn^{2+} + Fe^{2+} + \underset{\text{bicarbonate}}{HCO_3^-} + OH^- = \underset{\text{mixed carbonate}}{CaMnFe(CO_3)_3} + H_2O \qquad \textbf{10.}$$

This potential for mineral trapping, in combination with the heterogeneous nature and variable permeability of the unit, indicates the Hutton Sandstone could act as an effective secondary reservoir and seal unit (Figure 17), with internal baffling by finer-grained reactive units likely to slow the migration of CO_2 (Watson, 2006).

5.5.2 Evergreen Formation

Both samples from the Evergreen Formation contain moderate amounts of feldspars and chlorite, in addition to kaolin, micas and biotite-group minerals. During reaction, Fe was dissolved into reaction fluids for both samples. In spite of the very fine-grained, compacted nature of the sample and the negligible starting porosity, minor increase in porosity (from 0.2 to 1 % porosity) was observed in the lower Evergreen Formation sample (1138 m), primarily due to the dissolution of carbonates. Interestingly, although the coarser-grained Evergreen sample had higher porosity prior to reaction (2.0 vol. % vs. 0.2 vol. %), no increase in porosity was observed in this sample following CO_2 exposure. The contribution of substantial Fe to the formation fluid opens the possibility of siderite precipitation in the longer term, meaning the unit has the potential to become self-sealing at the fluid-rock interface due to the potential precipitation of siderite, Fe-oxihydroxides, ± amorphous silica.

Previous work by Watson et al. (2005) shows CO_2 reactions with clay-rich lithologies can improve the seal capacity of a unit through the precipitation of carbonate products. The very fine-grained intervals of the Evergreen Formation are likely to experience limited mixed fluid (CO_2 and water) reactions due to impeded penetration of fluids. This, in addition to the reactive mineralogy and high chlorite-smectite content, suggests the Evergreen Formation would be an effective seal unit. The heterogeneous nature of the unit is likely to see fluid penetration into the lower section of the formation, which is of poorer reservoir-quality (Figure 1). However, this could be beneficial in terms of CO_2 storage efficacy, as the internal heterogeneity and permeability variations are likely to result in tortuosity of the CO_2 migration path, leading to increased opportunity for CO_2 trapping to occur in the form of residual and mineral trapping.

5.5.3 Precipice Sandstone

The sample from the quartzose Precipice 1192 m is relatively unreactive, consisting predominantly of quartz, muscovite and poorly-reactive kaolin ± smectite clays. This, in combination with the high porosity (15–18 vol. %) of the sample, indicates the Precipice Sandstone is an attractive reservoir unit (Figure 17). During CO_2 reaction, the small increases in Fe, Ca and Si are attributed to partial dissolution of chlorite and remnant detrital plagioclase feldspars, and potentially to trace amounts of carbonate that were too fine-grained and sparse to be directly identified in petrographic studies. Due to this paucity of unstable mineral phases, no changes in porosity or permeability are expected during CO_2-water-rock reactions, and CO_2 trapping is likely to be limited to hydrodynamic trapping processes, in the form of residual and dissolution trapping. No precipitation of minerals is predicted to occur by kinetic geochemical modelling. Fluid-flow is expected to be controlled by internal permeability variations within the formation and hydraulic gradient, with CO_2 residence times in line with the hydrodynamic regime of the system.

5.5.4 Comparison with existing experimental studies

Whilst this study is the first to conduct freshwater CO_2-water-rock reactions at simulated in situ conditions, several previous studies have conducted similar batch reaction experiments at either low-pressure, low-salinity conditions, or high-pressure, high-salinity conditions, allowing comparison

between the different conditions. In general, similarities between the element release mechanisms (i.e. dissolution and desorption of minerals) are observed between the saline and freshwater studies, with differences observed in precipitation and extent of dissolution appearing to partly relate to rock composition, in addition to starting water chemistry and P-T conditions. Batch experiments conducted in saline conditions at similar or higher P-T reservoir conditions generally note similar element mobilisation mechanisms, with these studies identifying dissolution of minerals like feldspars, carbonates, clay minerals and anhydrite. Mineral precipitation observed in saline experiments include clay-like aluminosilicates, secondary calcite, kaolinite, gypsum, Fe-oxi/hydroxides, albite, silica and anhydrite (Rochelle et al., 2004; Bertier et al., 2006). During the study at similar reservoir P-T conditions by Wigand et al (2008), where flow-through experiments at 1 M NaCl, 30 °C and 15 MPa pore-fluid pressure conditions were undertaken, a decrease in pH and dissolution of carbonate cement was observed after CO_2 influx, with dissolution of feldspars occurring later in the experiment. However, unlike in the current study, Wigand et al (2008) also observed the precipitation of montmorillonite, although they were not able to reproduce this with modelling. Kaszuba et al. (2003) and Kaszuba et al. (2005) conducted more saline (5.5 molal) batch reactions at higher P-T conditions (200 °C and 200 bars), and observed magnesite ± siderite precipitation, considerable silicate dissolution of feldspars, biotite, and even quartz, and desiccation of brine after CO_2 injection in an Mg-bearing brine study (Kaszuba et al., 2003), suggesting formation salinity and P-T conditions have a considerable impact on CO_2-water-rock interactions, in addition to the initial host-rock mineralogy. In freshwater batch reaction studies by Smyth et al. (2009), Little and Jackson (2010), Lu et al. (2010), Humez et al. (2013), and Varadharajan et al. (2013), similar observations were made in the form of pH decrease and element mobilisation following CO_2 introduction. Despite differences in sample composition and preparation (i.e. using disaggregated rock or sediment) and P-T conditions (e.g. low-temperature, atmospheric pressure conditions) of the existing studies, in both our study and in previous low-salinity studies, following CO_2 injection, pH generally dropped by ~1–2 units (e.g. Kharaka et al., 2010; Little and Jackson, 2010; Lu et al., 2010; Zheng et al., 2012), with a pH drop of up to 3 units seen in poorly-buffered units (Trautz et al., 2013). Similarly, in both our study and

previous studies, this decrease in pH resulted in elevated levels of major and trace metal concentrations, such as Ca, Mg, Mn, Fe and Sr, due to dissolution, desorption and/or cation exchange on mineral surfaces. No precipitation of minerals is directly observed in the low-salinity experiments, although potential kaolinite precipitation is indicated in our study, and potential Fe-oxide (Lu et al., 2010; Cahill and Jakobsen, 2013) and clay precipitation (Lu et al., 2010) is indicated in other freshwater studies. From these studies, the importance of host-rock composition and pH buffering on the geochemical response of the system is highlighted, with carbonates identified as having the highest capacity to buffer pH in all studies.

6. CONCLUSIONS

Batch-reaction experiments under in situ Surat Basin conditions (T = 60 °C, P = 120 bar) have shown that injection and dissolution of CO_2 into low-salinity formations will result in geochemical reactions that are dependent on the host-rock lithology. Incremental fluid samples obtained during batch reaction of rock samples infer CO_2-water-rock interactions from changes in analyte concentrations. During CO_2 reaction, the majority of major and minor elements showed an overall increase in concentration with respect to initial water chemistry, indicating dissolution ± desorption of material into the fluid phase with decreasing pH, whilst decreases in element concentration in some effluent samples suggest the fluid is reaching a state of mineral saturation. Carbonates are observed to rapidly dissolve in the early stages of the experiment, whilst silicate minerals appear to follow a more gradual, linear dissolution trend. These dissolution and desorption processes are highly dependent on initial host rock mineralogy and lithology, with poorly-reactive samples showing little change in mineralogy.

Rock sample characterisation before and after CO_2 exposure allows insight into the impact of CO_2 reaction in low-salinity formation waters, with changes in porosity and mineralogy observed following reactions with supercritical CO_2. In general, negligible to minor porosity increases, or even decreases, were observed where fluid chemistry changes were largely attributed to the dissolution or desorption of silicate minerals (e.g. Fe-chlorites, annite, feldspars), especially in the finer-grained,

clay-rich intervals. In contrast, dissolution of carbonates in the carbonate-rich samples resulted in a considerable increase in porosity, which is likely to substantially improve permeability. As a result, the starting mineralogical composition of a reservoir unit is likely to have a large impact on the evolution of reservoir quality characteristics during CO_2 injection and storage. In addition, by comparing the results of this study with previous saline and low-salinity experiments at various P-T conditions, it is evident that rock composition is one of the major factors that influences CO_2-water-rock interactions, in addition to formation water chemistry and P-T conditions.

The implications of CO_2-water-rock interactions in the low-salinity Surat Basin reveal a potential reservoir system comprising a clean, poorly-reactive primary seal unit, a heterogeneous and reactive seal unit, and an overlying internally baffled dual reservoir-seal unit (Figure 17). Initial reactions expected to take place are the partial dissolution of calcite, mixed carbonates, chlorite and chloritic clays, and annite, followed in the longer-term by the dissolution of additional silicates, such as plagioclase and alkali feldspar. Rapid dissolution of Ca-, Fe- and Mn-bearing carbonates is expected to improve injectivity in the near-well environment, and contribute to the eventual re-trapping of CO_2 in the form of re-precipitation of carbonates, especially in the internally-baffled intervals of the Evergreen Formation and Hutton Sandstone, where CO_2 is likely to be slowed by tortuosity held by capillary trapping. Although understanding the long-term interactions in low-salinity CO_2 storage systems will necessitate long-term experimental investigations and kinetic geochemical modelling, short-term experiments can provide valuable information on near bore-well CO_2-water-rock interactions. Detailed characterisation of core samples prior to and following CO_2 exposure—as is presented in this study—will likely result in a good agreement between experiment outcomes and modelled predictions. This is vital when building models for predicting site-scale interactions during CO_2 injection and storage.

7. ACKNOWLEDGEMENTS

The authors thank The Australian National Low Emissions Coal Research and Development (ANLEC R&D) and Carbon Transport and Storage Company (CTSCo) for sponsoring this research. ANLEC

R&D is supported by Australian Coal Association Low Emissions Technology Limited and the Australian Government through the Clean Energy Initiative. Julie Pearce acknowledges the funding provided by the Commonwealth of Australia and industry sponsors through the CO2CRC Program. We would like to acknowledge and thank Lithicon for access to micro-CT data. Technical support was kindly provided by Victor Rudolph, Anastasia Dmyterko, Marietjie Mosert and Guia Morelli. Ulrike Schacht (Australian School of Petroleum) is thanked for performing microprobe analyses. The authors acknowledge the facilities, and the scientific and technical assistance, of the Australian Microscopy & Microanalysis Research Facility at the Centre for Microscopy and Microanalysis, The University of Queensland. Finally, we express our gratitude to those who provided helpful and supportive feedback to improve our manuscript, in particular our two anonymous reviewers.

8. REFERENCES

Almond, C.S., 1985. Well completion report, GSQ Chinchilla 4. Geological Survey of Queensland.

Apps, J., Zheng, L., Zhang, Y., Xu, T., Birkholzer, J., 2010. Evaluation of potential changes in groundwater quality in response to CO_2; leakage from deep geologic storage. Transport in Porous Media, 82(1): 215–246.

Assayag, N., Matter, J., Ader, M., Goldberg, D., Agrinier, P., 2009. CO_2 ionic trapping at meta-sedimentary aquifer, following a CO_2 injection push-pull test. Energy Procedia, 1(1): 2357–2360.

Bachu, S., 2000. Sequestration of CO_2 in geological media: criteria and approach for site selection in response to climate change. Energy Conversion and Management, 41(9): 953–970.

Bachu, S., Bennion, B., 2008. Effects of in-situ conditions on relative permeability characteristics of CO_2-brine systems. Environmental Geology, 54(8): 1707–1722.

Bachu, S., Bonijoly, D., Bradshaw, J., Burruss, R., Holloway, S., Christensen, N.P., Mathiassen, O.M., 2007. CO_2 storage capacity estimation: Methodology and gaps. International Journal of Greenhouse Gas Control, 1: 430–443.

Bachu, S., Gunter, W.D., Perkins, E.H., 1994. Aquifer disposal of CO_2: Hydrodynamic and mineral trapping. Energy Conversion and Management, 35(4): 269–279.

Beig, M.S., Lüttge, A., 2006. Albite dissolution kinetics as a function of distance from equilibrium: Implications for natural feldspar weathering. Geochimica et Cosmochimica Acta, 70(6): 1402–1420.

Benson, S., Cook, P., 2006. Chapter 5 - Underground geological storage. In: Metz, B., Davidson, O., De Coninck, H., Loos, M., Meyer, L. (Eds.), IPCC Special report on carbon dioxide capture and storage, pp. 195–276.

Bertier, P., Swennen, R., Laenen, B., Lagrou, D., Dreesen, R., 2006. Experimental identification of CO_2–water–rock interactions caused by sequestration of CO_2 in Westphalian and Buntsandstein sandstones of the Campine Basin (NE-Belgium). Journal of Geochemical Exploration, 89(1–3): 10–14.

Bethke, C.M., Yeakel, S., 2013. The Geochemist's Workbench Realease 9.0: Reaction Modeling Guide, Aqueous Solutions, LLC, Champaign, Illinois.

Biddle, K.T., Wielchowsky, C.C. (Eds.), 1994. Hydrocarbon traps. The petroleum system—from source to trap, AAPG Memoir, 60. American Association of Petroleum Geologists, Tulsa.

Birkholzer, J.T., Zhou, Q., Tsang, C.-F., 2009. Large-scale impact of CO_2 storage in deep saline aquifers: A sensitivity study on pressure response in stratified systems. International Journal of Greenhouse Gas Control, 3(2): 181–194.

Bradshaw, B.E., Spencer, L.K., Lahtinen, A.C., Khider, K., Ryan, D.J., Colwell, J.B., Chirinos, A., Bradshaw, J., 2009. Queensland carbon dioxide geological storage atlas.

Cahill, A.G., Jakobsen, R., 2013. Hydro-geochemical impact of CO_2 leakage from geological storage on shallow potable aquifers: A field scale pilot experiment. International Journal of Greenhouse Gas Control, 19(0): 678–688.

Carlson, W.D., Rowe, T., Ketcham, R.A., Colbert, M.W., 2003. Applications of high-resolution X-ray computed tomography in petrology, meteoritics and palaeontology. In: Mees, F., Swennen, R., Van Geet, M., Jacobs, P. (Eds.), Applications of X-ray Computed Tomography in the Geosciences. Geological Society, London, Special Publications, pp. 7–22.

Civan, F., 2007. Reservoir Formation Damage: Fundamentals, Modeling, Assessment, and Mitigation. Elsevier Inc.

Cresswell, R.G., Smerdon, B.D., Rousseau-Gueutin, P., Simon, S., Taylor, A.R., Davies, P.J., Habermehl, M.A., 2012. Chapter 6: Hydrodynamics. In: Smerdon, B.D., Ransley, T.R. (Eds.), Water resource assessment for the Surat region. A report to the Australian Government from the CSIRO Great Artesian Basin Water Resource Assessment. CSIRO Water for a Healthy Country Flagship, Australia.

Davidson, P.M., 1994. Ternary iron, magnesium, calcium carbonates; a thermodynamic model for dolomite as an ordered derivative of calcite-structure solutions. American Mineralogist, 79(3–4): 332–339.

Dawson, G.K.W., Pearce, J.K., Biddle, D., Golding, S.D., 2014. Experimental mineral dissolution in Berea Sandstone reacted with CO_2 or SO_2-CO_2 in NaCl brine under CO_2 sequestration conditions. Chemical Geology, in prep (this issue).

Delany, J.M., Lundeen, S.R., 1989. The LLNL thermodynamic database, Lawrence Livermore National Laboratory Report UCRL-21658.

Duan, Z., Sun, R., 2003. An improved model calculating CO2 solubility in pure water and aqueous NaCl solutions from 273 to 533 K and from 0 to 2000 bar. Chemical Geology, 193(3–4): 257–271.

Farquhar, S.M., Dawson, G.K.W., Esterle, J.S., Golding, S.D., 2013. Mineralogical characterisation of a potential reservoir system for CO_2 sequestration in the Surat Basin. Australian Journal of Earth Sciences, 60(1): 91–110.

Gaus, I., 2010. Role and impact of CO_2–rock interactions during CO_2 storage in sedimentary rocks. International Journal of Greenhouse Gas Control, 4(1): 73–89.

Gibson-Poole, C.M., Root, R.S., Lang, S.C., Streit, J.E., Hennig, A.L., Otto, C.J., Underschultz, J., 2005. Conducting comprehensive analyses of potential sites for geological CO_2 storage. In: Rubin, E., Keith, D., Gilboy, C. (Eds.), Proceedings of the 7th international conference on greenhouse gas control technologies. Elsevier, Vancouver, pp. 673–681.

Golab, A., Romeyn, R., Averdunk, H., Knackstedt, M., Senden, T.J., 2012. 3D characterisation of potential CO2 reservoir and seal rocks. Australian Journal of Earth Sciences, 60(1): 111–123.

Golab, A., Ward, C.R., Permana, A., Lennox, P., Botha, P., 2013. High-resolution three-dimensional imaging of coal using microfocus X-ray computed tomography, with special reference to modes of mineral occurrence. International Journal of Coal Geology, 113(0): 97–108.

Golab, A.N., Knackstedt, M.A., Averdunk, H., Senden, T., Butcher, A.R., Jaime, P., 2010. 3D porosity and mineralogy characterization in tight gas sandstones. The Leading Edge, 29(12): 1476–1483.

Gunter, W.D., Perkins, E.H., McCann, T.J., 1993. Aquifer disposal of CO_2-rich gases: Reaction design for added capacity. Energy Conversion and Management, 34(9-11): 941–948.

Gunter, W.D., Wiwehar, B., Perkins, E.H., 1997. Aquifer disposal of CO_2-rich greenhouse gases: Extension of the time scale of experiment for CO_2-sequestering reactions by geochemical modelling. Mineralogy and Petrology, 59(1): 121–140.

Herron, M.M., 1988. Geochemical classification of terrigenous sands and shales from core or log data. Journal of Sedimentary Research, 58(5): 820–829.

Hodginkson, J., Preda, M., Hortle, A., McKillop, M., Dixon, O., Foster, L., 2009. The potential impact of carbon dioxide injection on freshwater aquifers: the Surat and Eromanga Basins in Queensland. Queensland Minerals and Energy Review, 16: 133.

Hodgkinson, J., Grigorescu, M., 2012. Background research for selection of potential geostorage targets—case studies from the Surat Basin, Queensland. Australian Journal of Earth Sciences: 1–19.

Holland, T., Baker, J., Powell, R., 1998. Mixing properties and activity-composition and relationships of chlorites in the system MgO-FeO-Al 2 O 3 -SiO 2 -H 2 O. European Journal of Mineralogy, 10(3): 395–406.

Holloway, S., 2009. Storage capacity and containment issues for carbon dioxide capture and geological storage on the UK Continental Shelf. Proceedings of the Institution of Mechanical Engineers, Part A: Journal of Power and Energy, 223: 239–248.

Hovorka, S.D., Choi, J.-W., Meckel, T.A., Trevino, R.H., Zeng, H., Kordi, M., Wang, F.P., Nicot, J.-P., 2009. Comparing carbon sequestration in an oil reservoir to sequestration in a brine formation--field study. Energy Procedia, 1(1): 2051–2056.

Humez, P., Lagneau, V., Lions, J., Negrel, P., 2013. Assessing the potential consequences of CO_2 leakage to freshwater resources: A batch-reaction experiment towards an isotopic tracing tool. Applied Geochemistry, 30(0): 178–190.

Kaldi, J.G., Gibson-Poole, C.M., 2008. Storage capacity estimation, site selection and characterisation for CO_2 Storage Projects. Report No. RPT08-1001. CO2CRC, Canberra, 52 pp.

Kaszuba, J.P., Janecky, D.R., Snow, M.G., 2003. Carbon dioxide reaction processes in a model brine aquifer at 200 °C and 200 bars: implications for geologic sequestration of carbon. Applied Geochemistry, 18(7): 1065–1080.

Kaszuba, J.P., Janecky, D.R., Snow, M.G., 2005. Experimental evaluation of mixed fluid reactions between supercritical carbon dioxide and NaCl brine: Relevance to the integrity of a geologic carbon repository. Chemical Geology, 217(3–4): 277–293.

Kellett, J.R., Radke, B.M., Ransley, T.R., Bell, J.G., Stewart, G.A., 2012. Chapter 5: Hydrogeological framework. In: Smerdon, B.D., Ransley, T.R. (Eds.), Water resource assessment for the Surat region. A report to the Australian Government from the CSIRO Great Artesian Basin Water Resource Assessment. CSIRO Water for a Healthy Country Flagship, Australia.

Ketzer, J.M., Iglesias, R., Einloft, S., Dullius, J., Ligabue, R., de Lima, V., 2009. Water–rock–CO_2 interactions in saline aquifers aimed for carbon dioxide storage: Experimental and numerical modeling studies of the Rio Bonito Formation (Permian), southern Brazil. Applied Geochemistry, 24(5): 760–767.

Kharaka, Y., Thordsen, J., Kakouros, E., Ambats, G., Herkelrath, W., Beers, S., Birkholzer, J., Apps, J., Spycher, N., Zheng, L., Trautz, R., Rauch, H., Gullickson, K., 2010. Changes in the chemistry of shallow groundwater related to the 2008 injection of CO_2 at the ZERT field site, Bozeman, Montana. Environmental Earth Sciences, 60(2): 273-284.

Knackstedt, M., Carnerup, A., Golab, A., Sok, R., Young, B., Riepe, L., 2013. Petrophysical characterization of unconventional reservoir core at multiple scales. Petrophysics, 54(3): 216–223.

Koide, H., Tazaki, Y., Noguchi, Y., Nakayama, S., Iijima, M., Ito, K., Shindo, Y., 1992. Subterranean containment and long-term storage of carbon dioxide in unused aquifers and in depleted natural gas reservoirs. Energy Conversion and Management, 33(5–8): 619–626.

Lico, M.S., Kharaka, Y.K., Carothers, W.W., Wright, V.A., 1982. Methods for collection and analysis of geopressured geothermal and oil field waters. Water Supply Paper 2194. U.S. Geological Survey, Washington : U.S. G.P.O., 21 pp.

Little, M.G., Jackson, R.B., 2010. Potential impacts of leakage from deep CO_2 geosequestration on overlying freshwater aquifers. Environmental Science & Technology, 44(23): 9225–9232.

Lu, J., Partin, J.W., Hovorka, S.D., Wong, C., 2010. Potential risks to freshwater resources as a result of leakage from CO_2 geological storage: A batch-reaction experiment. Environmental Earth Sciences, 60(2): 335–348.

Luquot, L., Andreani, M., Gouze, P., Camps, P., 2012. CO_2 percolation experiment through chlorite/zeolite-rich sandstone (Pretty Hill Formation – Otway Basin–Australia). Chemical Geology, 294–295(0): 75–88.

Michael, K., Arnot, M., Cook, P.J., Ennis-King, J., Funnell, R., Kaldi, J., Kirste, D., Paterson, L., 2009. CO2 storage in saline aquifers I—current state of scientific knowledge. Energy Procedia, 1: 3197–3204.

Nicot, J.-P., 2008. Evaluation of large-scale CO_2 storage on fresh-water sections of aquifers: An example from the Texas Gulf Coast Basin. International Journal of Greenhouse Gas Control, 2(4): 582–593.

Pearce, J.K., Kirste, D.M., Dawson, G.W., Farquhar, S.M., Biddle, D., Golding, S.D., Rudolph, V., 2014. SO_2 impurity impacts on experimental and simulated CO_2-water-reservoir rock reactions at carbon storage conditions. Chemical Geology, in prep (this issue).

Pettijohn, F.J., Potter, P.E., Siever, R., 1987. Sand and Sandstone. Springer Science+Business Media, New York, 618 pp.

Potter, P.E., 1978. Petrology and chemistry of modern big river sands. The Journal of Geology, 86(4): 423–449.

Raza, A., Hill, K.C., Korsch, R.J., 2009. Mid-Cretaceous uplift and denudation of the Bowen and Surat Basins, eastern Australia: Relationship to Tasman Sea rifting from apatite fission-track and vitrinite-reflectance data. Australian Journal of Earth Sciences, 56(3): 501–531.

Rochelle, C.A., Czernichowski-Lauriol, I., Milodowski, A.E., 2004. The impact of chemical reactions on CO_2 storage in geological formations: a brief review. Geological Society, London, Special Publications, 233(1): 87–106.

Rosenbauer, R.J., Koksalan, T., 2002. Experimental determination of the solubility of CO_2 in electrolytes: Application to CO_2 sequestration in deep, saline aquifers, Geological society of America Annual Meeting, GSA, Denver, Colorado.

Rosenbauer, R.J., Koksalan, T., Palandri, J.L., 2005. Experimental investigation of CO_2–brine–rock interactions at elevated temperature and pressure: Implications for CO_2 sequestration in deep-saline aquifers. Fuel Processing Technology, 86(14–15): 1581–1597.

Shukla, R., Ranjith, P., Haque, A., Choi, X., 2010. A review of studies on CO_2 sequestration and caprock integrity. Fuel, 89(10): 2651–2664.

Smyth, R.C., Hovorka, S.D., Lu, J., Romanak, K.D., Partin, J.W., Wong, C., Yang, C., 2009. Assessing risk to fresh water resources from long term CO_2 injection–laboratory and field studies. Energy Procedia, 1(1): 1957–1964.

Solomon, S., Carpenter, M., Flach, T.A., 2008. Intermediate storage of carbon dioxide in geological formations: A technical perspective. International Journal of Greenhouse Gas Control, 2(4): 502–510.

Trautz, R.C., Pugh, J.D., Varadharajan, C., Zheng, L., Bianchi, M., Nico, P.S., Spycher, N.F., Newell, D.L., Esposito, R.A., Wu, Y., Dafflon, B., Hubbard, S.S., Birkholzer, J.T., 2013. Effect of dissolved CO_2 on a shallow groundwater system: A controlled release field experiment. Environmental Science & Technology, 47(1): 298–305.

Varadharajan, C., Tinnacher, R.M., Pugh, J.D., Trautz, R.C., Zheng, L., Spycher, N.F., Birkholzer, J.T., Castillo-Michel, H., Esposito, R.A., Nico, P.S., 2013. A laboratory study of the initial effects of dissolved carbon dioxide (CO_2) on metal release from shallow sediments. International Journal of Greenhouse Gas Control, 19(0): 183–211.

Watson, M.N., 2006. Petrological characterisation of the Vlaming Sub-Basin, Perth Basin for the purpose of CO_2 storage, CO2CRC report number RPT06-0098.

Watson, M.N., Daniel, R.F., Tingate, P.R., Gibson-Poole, C.M., 2005. CO_2 related seal capacity enhancement in mudstones: evidence from the Pine Lodge natural CO_2 accumulation, Otway Basin, Australia. In: Rubin, E.S., Keith, D.W., Gilboy, C.F. (Editors), 7th international Conference on Greenhouse Gas Control Technologies, Vancouver, Canada.

Wigand, M., Carey, J.W., Schütt, H., Spangenberg, E., Erzinger, J., 2008. Geochemical effects of CO_2 sequestration in sandstones under simulated in situ conditions of deep saline aquifers. Applied Geochemistry, 23(9): 2735–2745.

Wilke, F.D.H., Vásquez, M., Wiersberg, T., Naumann, R., Erzinger, J., 2012. On the interaction of pure and impure supercritical CO_2 with rock forming minerals in saline aquifers: An experimental geochemical approach. Applied Geochemistry, 27(8): 1615–1622.

Yu, Z., Liu, L., Yang, S., Li, S., Yang, Y., 2012. An experimental study of CO_2–brine–rock interaction at in situ pressure–temperature reservoir conditions. Chemical Geology, 326–327(0): 88–101.

Zheng, L., Apps, J.A., Spycher, N., Birkholzer, J.T., Kharaka, Y.K., Thordsen, J., Beers, S.R., Herkelrath, W.N., Kakouros, E., Trautz, R.C., 2012. Geochemical modeling of changes in shallow groundwater chemistry observed during the MSU-ZERT CO_2 injection experiment. International Journal of Greenhouse Gas Control, 7(0): 202–217.

FIGURE CAPTIONS

Figure 1: Overview of the traditional Surat Basin CO_2 reservoir system. Formation depths based on the Chinchilla 4 study well. Lithological "reservoir quality" indicator adapted from gamma logs for the study well, presented in Bradshaw et al. (2009), which generally reflect mudstone vs. sandstone content.

Figure 2: Schematic of Surat Basin batch reactor CO_2-water-rock experiment setup. An internal view of the reaction vessel is provided; a supercritical gas phase head exists above the bulk water phase (shaded) containing saturated core samples. ISCO = injection pump, DA = data acquisition.

Figure 3: The process of digital core analysis: a) photo of sample sub-plug with dimensions, b) Vertical slice of 3D tomogram (resolution is 2.2 μm), c) high-resolution registered SEM (200× zoom), d) corresponding slice of 3D tomogram, e) registered QEMSCAN mineral map.

Figure 4: Geochemical classification of brother Surat Basin sandstone and siltstone samples to those selected for reaction with supercritical CO_2: a) modified from Pettijohn et al. (1987), and b) modified from Herron (1988). Samples labelled (D) represent duplicate analyses.

Figure 5: QEMSCAN mineral assays of polished sections from plugs prior to CO_2-water-rock reactions: a) Hutton 799 m, b) Hutton 867 m, c) Evergreen 897 m, d) Evergreen 1138 m, and e) Precipice 1192 m.

Figure 6: Evolution of pH of measured effluent during the CO_2 reaction experiments. Initial measurements, taken prior to t = 0, represent CO_2 blanks; measurements at t = 0 are taken following the N_2 soak, just prior to the addition of supercritical CO_2.

Figure 7: Aqueous cation concentrations in effluent fluids prior to and during CO_2-water-rock reactions for A- and B-run samples: a) Hutton 799 m, b) Hutton 867 m, c) Evergreen 897 m, d) Evergreen 1138 m, and e) Precipice 1192 m. Rock sample added to purified water with N_2 at t = −1. CO_2 introduced at t = 0. Symbol size ≥ associated 5 % error; connecting lines are for illustrative purposes only.

Figure 8: Aqueous concentration vs. time before and during CO_2-water-rock reaction experiments at simulated basin conditions: a) Ca, b) Mn, c) Sr and d) S. Rock sample added to purified water with N_2 at t = −1. CO_2 introduced at t = 0. Error bars are 5 %. Connecting lines are for illustrative purposes only.

Figure 9: Aqueous concentration vs. time before and during CO_2-water-rock reaction experiments at simulated basin conditions: a) Si, b) Fe, c) Mg, d) Al, e) K and f) Na. Rock sample added to purified water with N_2 at t = −1. CO_2 introduced at t = 0. Error bars are 5 %. Connecting lines are for illustrative purposes only.

Figure 10: 3D visualisation of Hutton Sandstone 799 m sub-plug from registered 3D tomograms, with arrows at points of interest: a) before CO_2 reaction, b) after CO_2 reaction, and c) the difference, or reacted material. Total calcite content of the subplug decreases from 17 vol. % to ~15 vol. % post-CO_2, for a total porosity increase of ~1 vol. %

Figure 11: SEM-EDS photomicrographs and spot analyses of Hutton Sandstone samples: Hutton 799 m a) calcite-cemented pre-CO_2, b) post-CO_2, and c) pre-CO_2 calcite spot analysis; Hutton 867 m d) pre-CO_2, e) Fe-chlorite post-CO_2, without carbonate, and f) K-feldspar post-CO_2. Q = quartz, Po = porosity, Ca = calcite, F = feldspar, Ka = kaolinite, Chl = chlorite, Smec = smectite, Kf = K-feldspar, An = annite, Ti = TiO_2.

Figure 12: SEM-EDS photomicrographs and spot analyses of Evergreen 897 m: a) chloritic clay pre-CO_2, and b) partially collapsed post-CO_2; c) ankerite in chlorite pre-CO_2, and d) ankerite partially dissolved post-CO_2. Q = quartz, Chl = chlorite, An = annite, Kf = K-feldspar, Pf = plagioclase feldspar, Ka = kaolinite, Ak = ankerite, Feo = Fe-oxides, Ti = TiO_2.

Figure 13: SEM-EDS micrographs and spot analyses for Evergreen 1138 m: a) pre-CO_2 reaction, and b) post-CO_2 reaction. Although texture commonly appears preserved after reaction, selective dissolution of trace carbonates is observed in some locations, seen here by a reduction in Ca in spot 3b (post-CO_2). Q = quartz, Ka = kaolinite, Kf = K-feldspar, An = annite, Pf = plagioclase feldspar, Ti-An = Ti-rich annite.

Figure 14: SEM-EDS photomicrographs and spot analysis of Precipice 1192 m: a) Quartz and kaolinite pre-CO_2, b) kaolinite pre-CO_2, and c) kaolinite post-CO_2. Q = quartz, Ka = kaolin, S = sulphides (Cu, Fe, Ca).

Figure 15: Predicted vs. measured experiment fluid composition evolution over time during B-run CO_2-water-rock reactions: a) Hutton 799 m, single-stage dissolution, with b) magnified view of low-concentration elements; c) Hutton 799 m, two-stage dissolution, with d) magnified view of low-concentration elements; e) Hutton 867 m; f) Evergreen 897 m; g) Evergreen 1138 m; and h) Precipice 1192 m.

Figure 16: Predicted mineral mass evolution over time during B-run CO_2-water-rock reactions: a) Hutton 799 m, with b) magnified view of low-concentration minerals, c) Hutton 867 m, d) Evergreen 897 m, e) Evergreen 1138 m, and f) Precipice 1192 m.

Figure 17: Schematic diagram of the Surat Basin as a low-salinity CO_2 storage system with theoretical interactions from injection: Precipice Sandstone as a clean porous primary reservoir; Evergreen Formation as a predominantly self-sealing, tight caprock; Hutton Sandstone as an internally-baffled, heterogeneous dual reservoir-seal unit. Formation depths based on the Chinchilla 4 study well. Lithological "reservoir quality" indicator adapted from gamma logs for the study well, presented in Bradshaw et al. (2009), which generally reflect mudstone vs. sandstone content.

TABLE CAPTIONS

Table 1: Summary of experiment and sampling procedure for each Surat Basin batch reactor CO_2-water-rock experiment run.

Table 2: Initial reactant masses and approximate dimensions of samples for experimental reaction with supercritical CO_2 and purified water at simulated Surat Basin reservoir conditions.

Table 3: Kinetic parameters used in geochemical modelling, as described in text and in detail by Pearce et al. (2014).

Table 4: Chemical composition (wt% oxides) of Jurassic-aged Surat Basin siliclastic samples.

Table 5: Resolved mineral and porosity components from 3D tomogram segmentation of the sub-plugs prior to CO_2-water-rock reactions (vol. %).

Table 6: Mineral assays (area %) of five Surat Basin samples derived from registered QEMSCAN microanalysis of polished sections from sub-plugs prior to CO_2-water-rock reactions.

Table 7: Microprobe compositions for selected minerals in Surat Basin samples.

Table 8: Changes in mass and skeletal (helium) density in rock offcuts following reaction with supercritical CO_2 and purified water at simulated Surat Basin reservoir conditions.

Table 9: Resolved summary mineralogy from QEMSCAN of a polished section through the sub-plug before and after reaction with supercritical CO_2 (area %).

Table 10: Resolved mineral and porosity components from 3D tomogram segmentation before and after reaction with supercritical CO_2 (vol. %).

Table 11: Initial rock mineralogy used in kinetic geochemical modelling of CO_2-water-rock experiments. Proportions are constrained by quantitative QEMSCAN, semi-quantitative XRD and SEM-EDS of pre-reaction samples or sister samples.

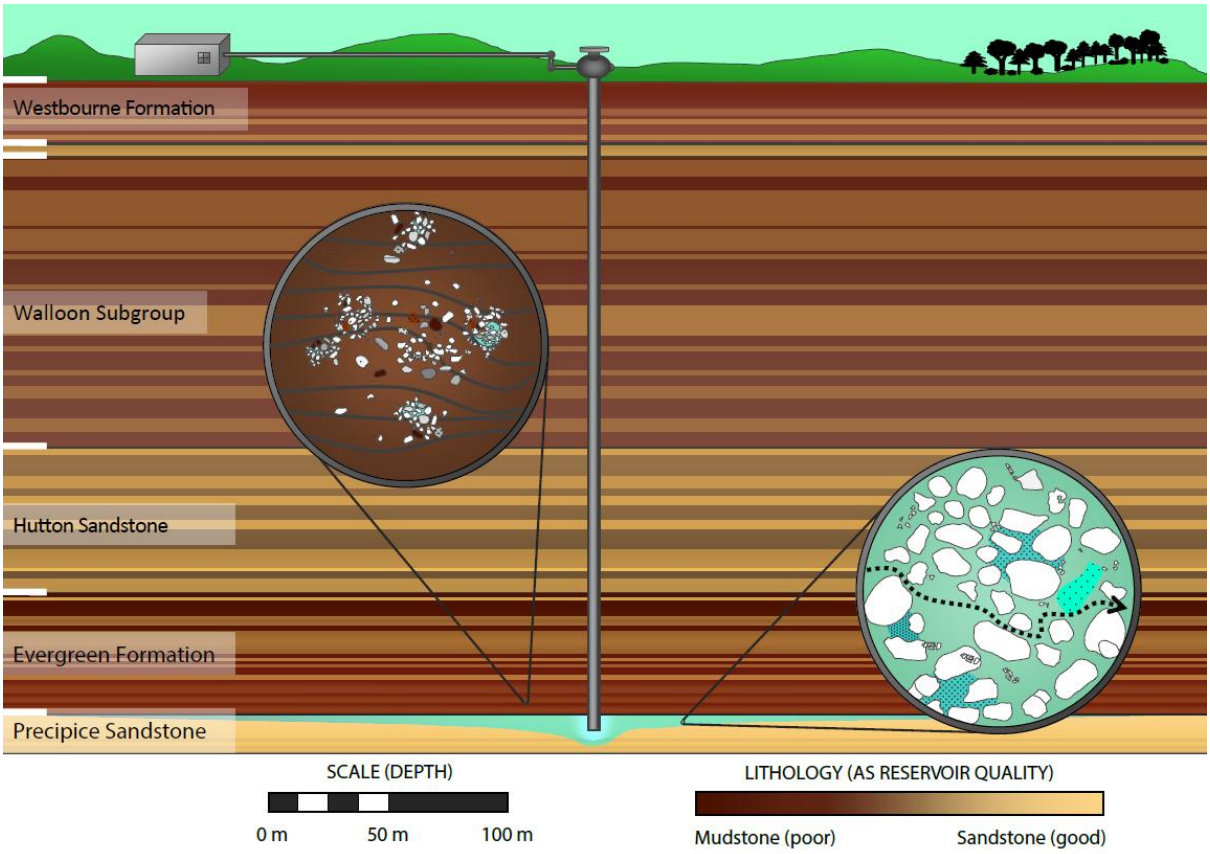

Figure 1

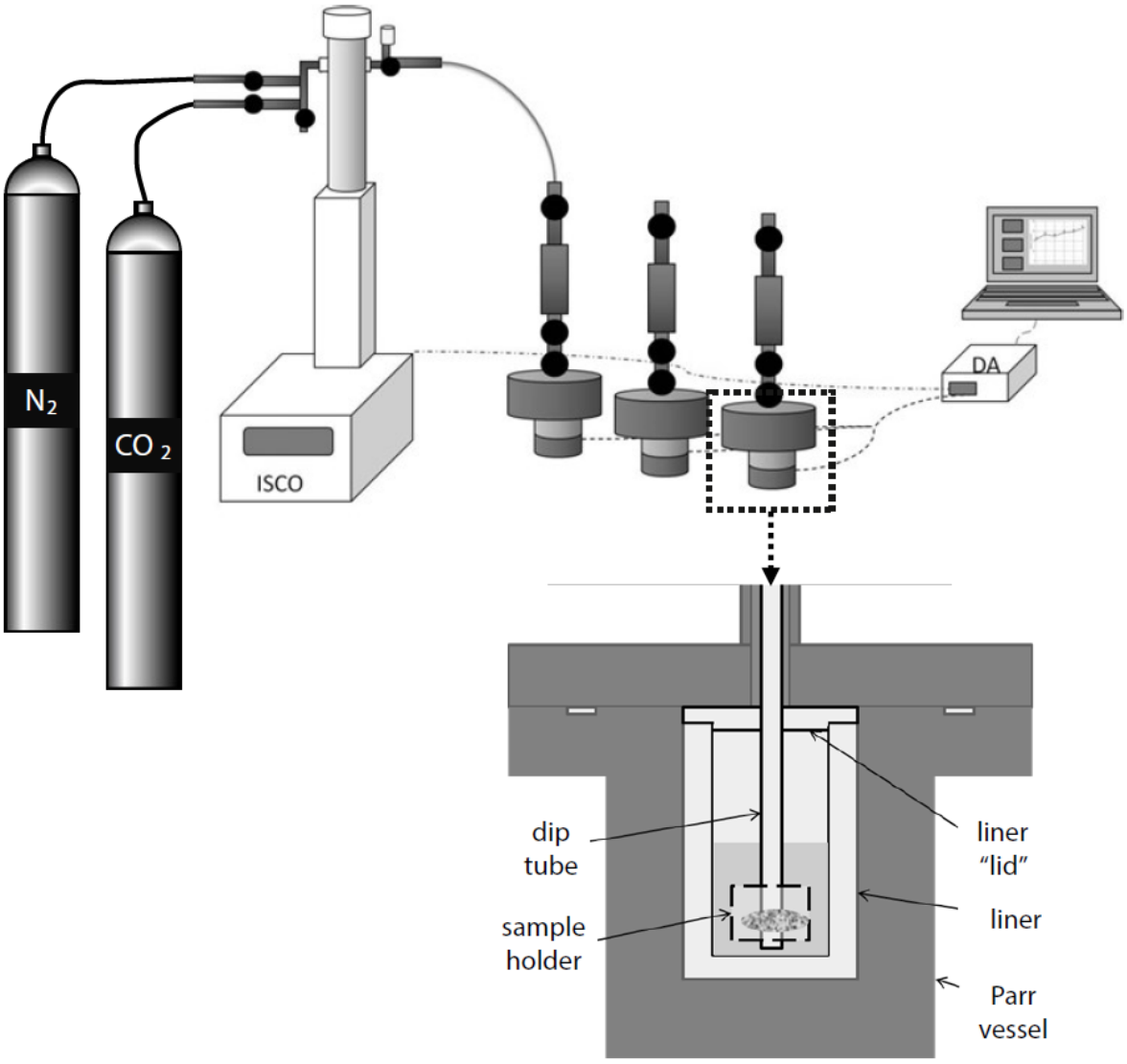

Figure 2

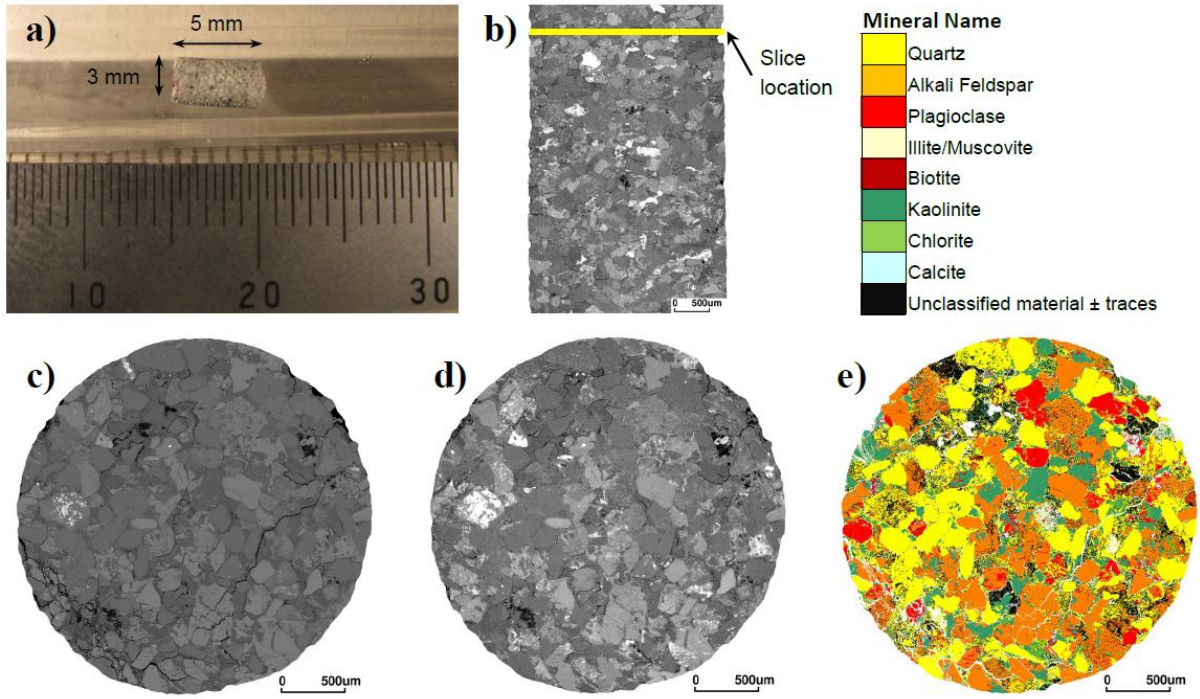

Figure 3

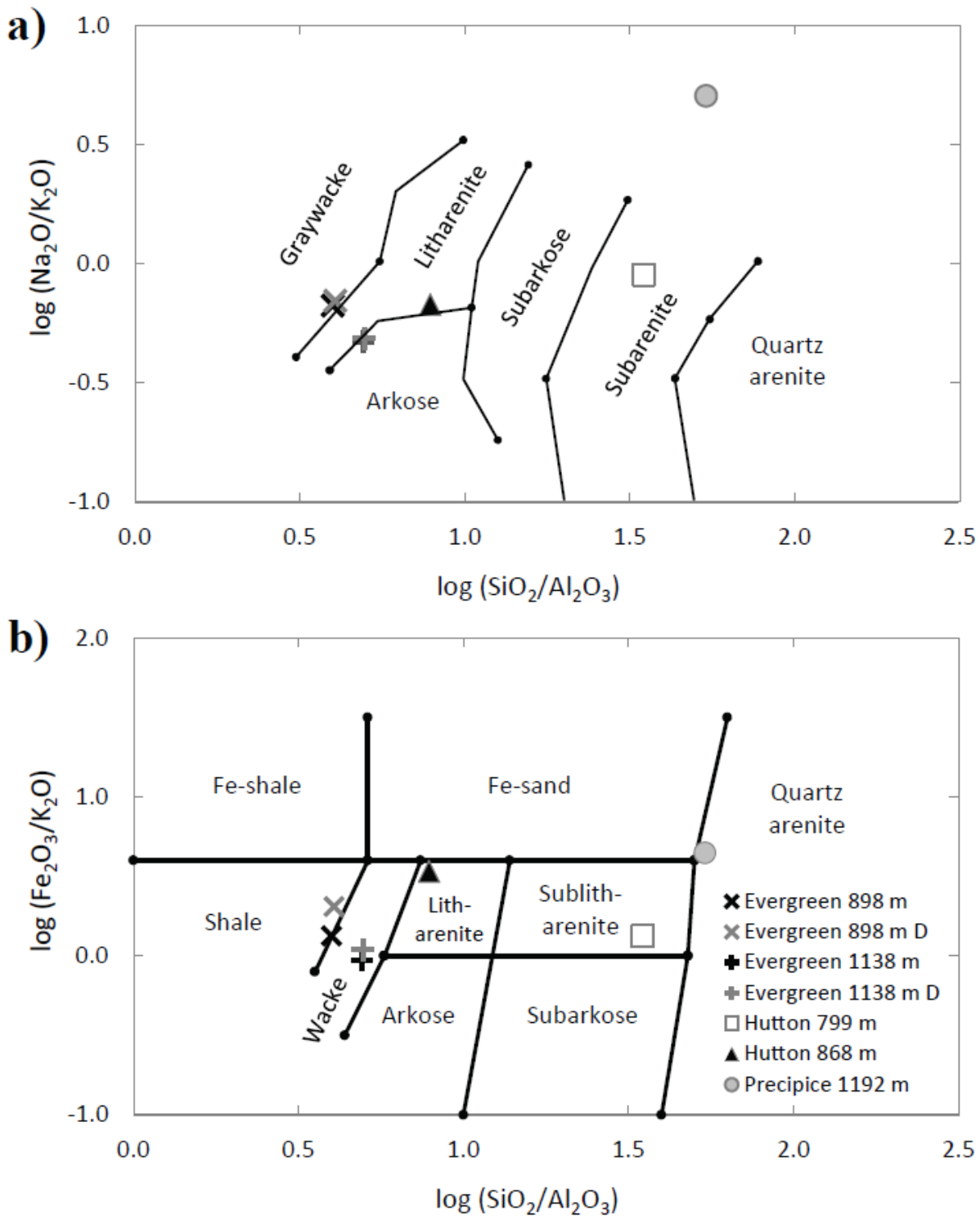
a)
1.0
0.5
0.0
-0.5
-1.0
0.0
0.5
1.0
1.5
2.0
2.5
log (Na2O/K2O)
log (SiO2/Al2O3)
Graywacke
Litharenite
Subarkose
Subarenite
Quartz arenite
Arkose
b)
2.0
1.0
0.0
-1.0
log (Fe2O3/K2O)
Fe-shale
Fe-sand
Quartz arenite
Shale
Lith-arenite
Sublith-arenite
Wacke
Arkose
Subarkose
Evergreen 898 m
Evergreen 898 m D
Evergreen 1138 m
Evergreen 1138 m D
Hutton 799 m
Hutton 868 m
Precipice 1192 m

Figure 4

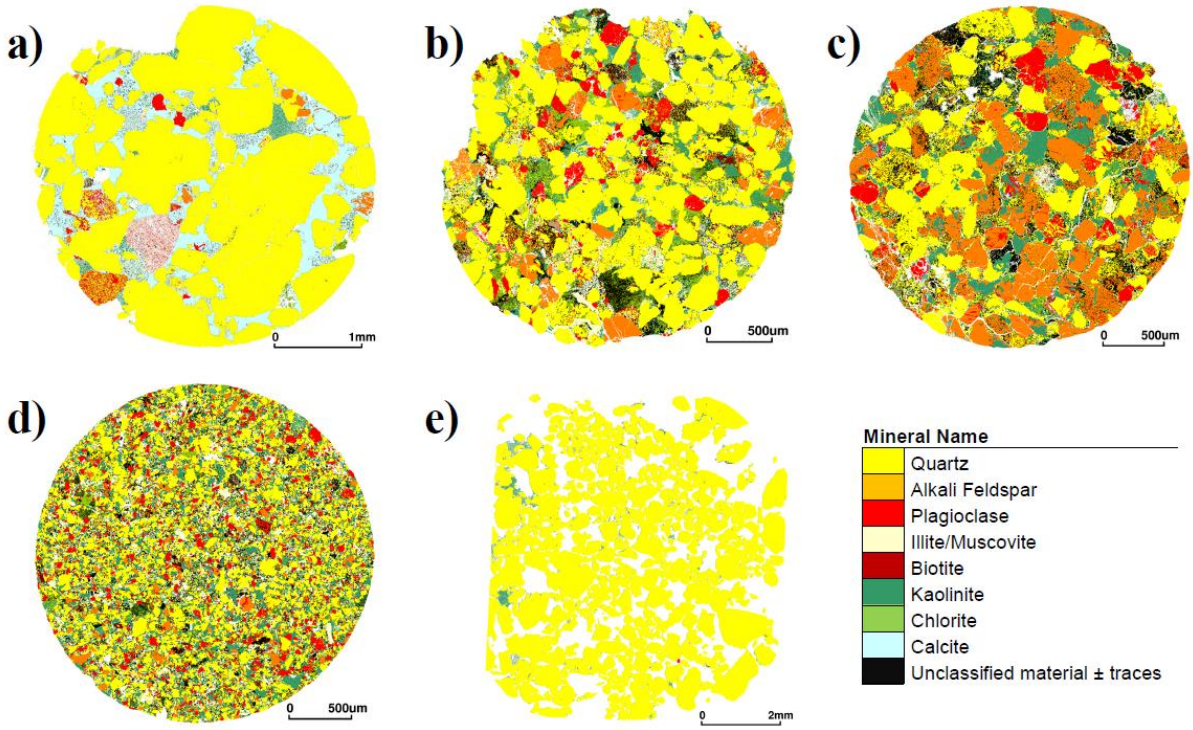

Figure 5

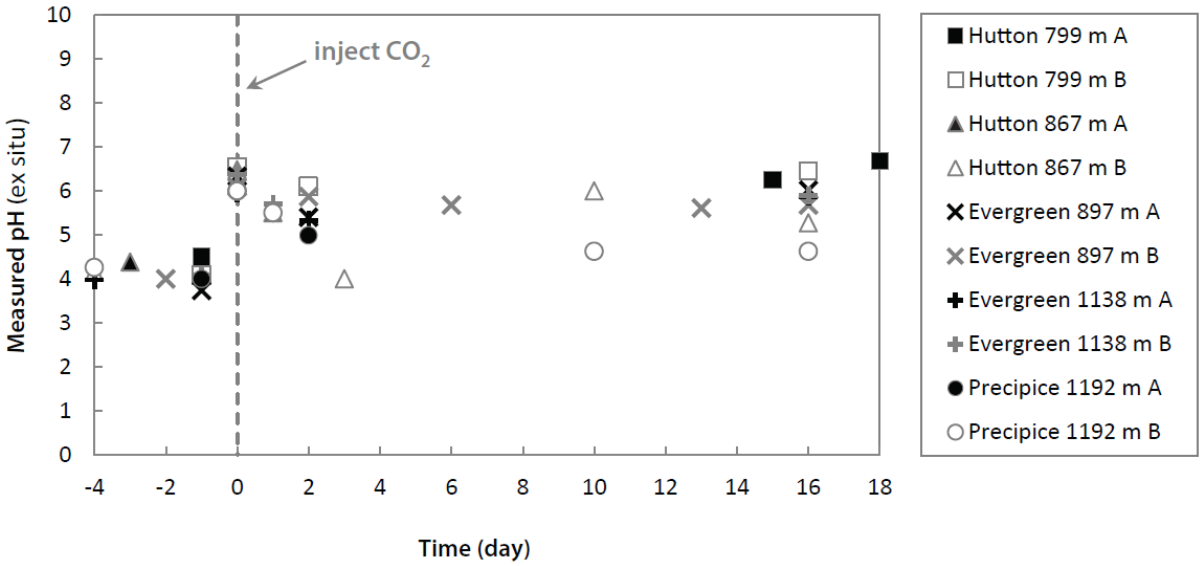

Figure 6

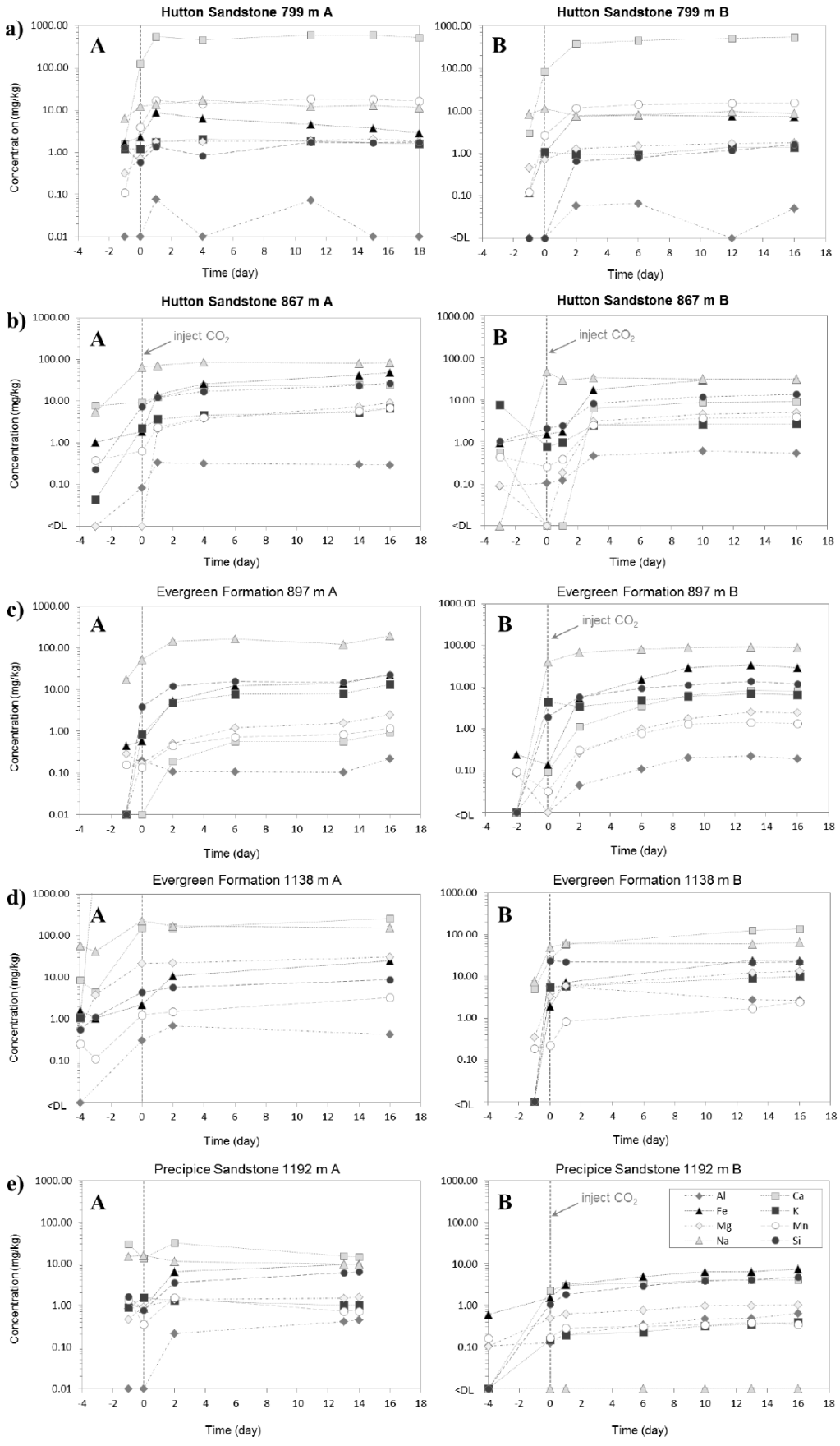
a)
Hutton Sandstone 799 m A
Hutton Sandstone 799 m B
b)
Hutton Sandstone 867 m A
Hutton Sandstone 867 m B
inject CO_2
c)
Evergreen Formation 897 m A
Evergreen Formation 897 m B
d)
Evergreen Formation 1138 m A
Evergreen Formation 1138 m B
e)
Precipice Sandstone 1192 m A
Precipice Sandstone 1192 m B
A
B
Concentration (mg/kg)
Time (day)
<DL
Al
Ca
Fe
K
Mg
Mn
Na
Si

Figure 7

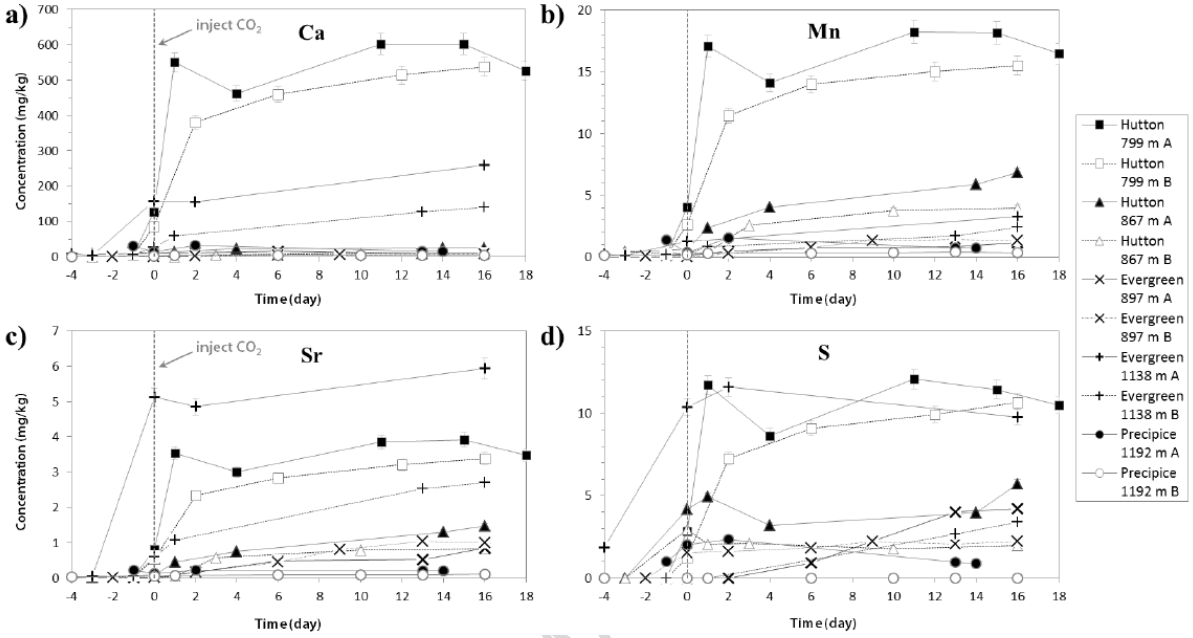

Figure 8

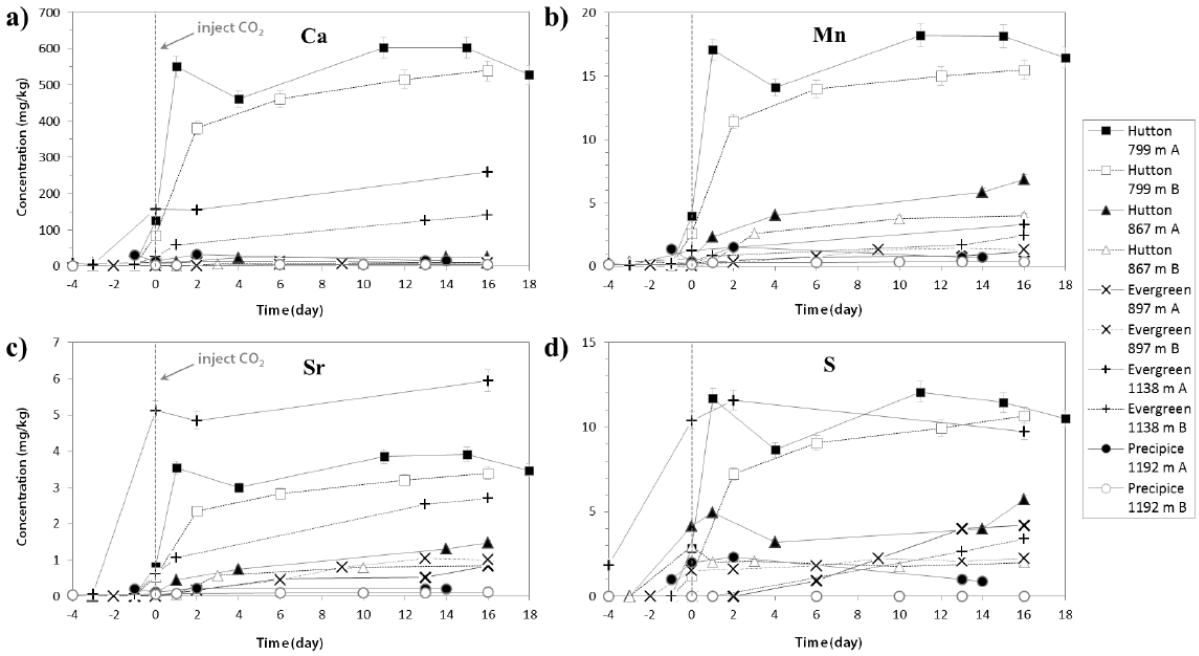

Figure 9

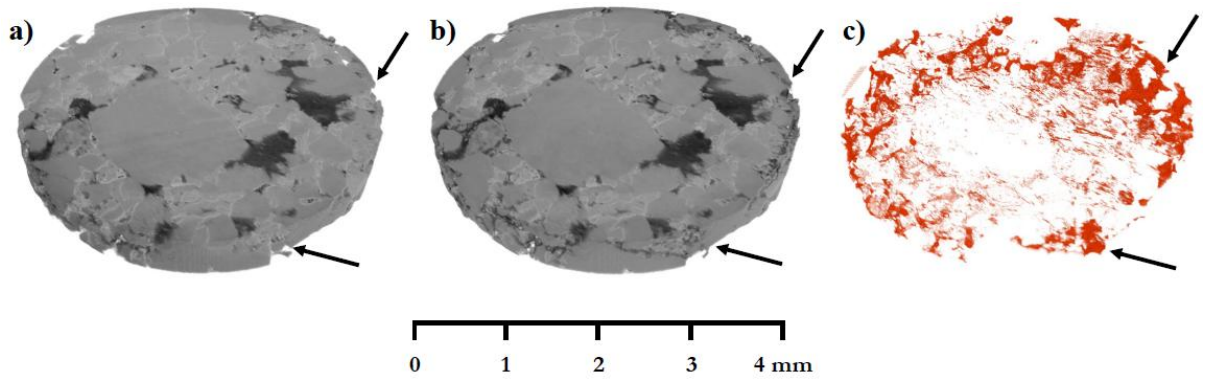

Figure 10

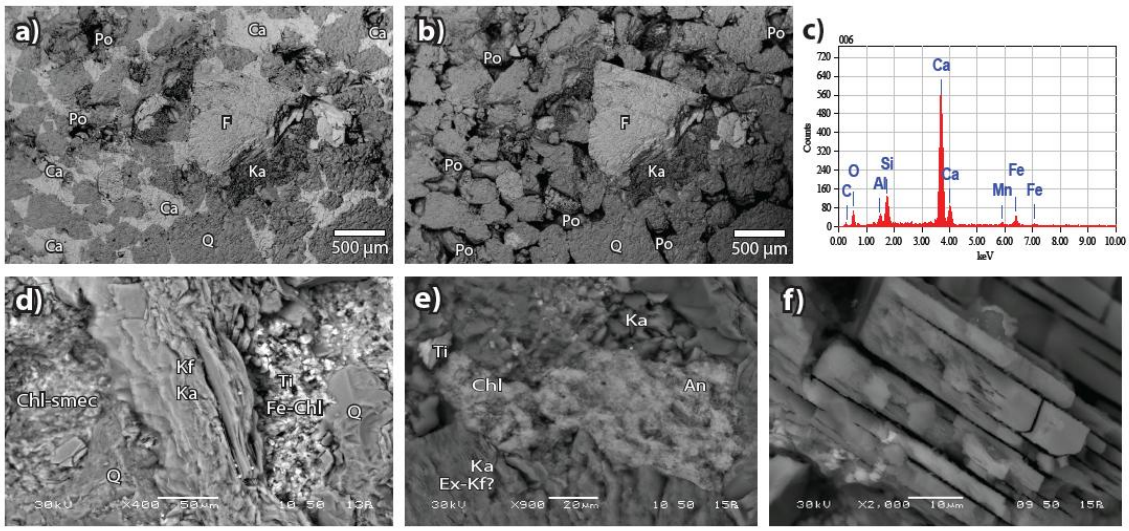

Figure 11

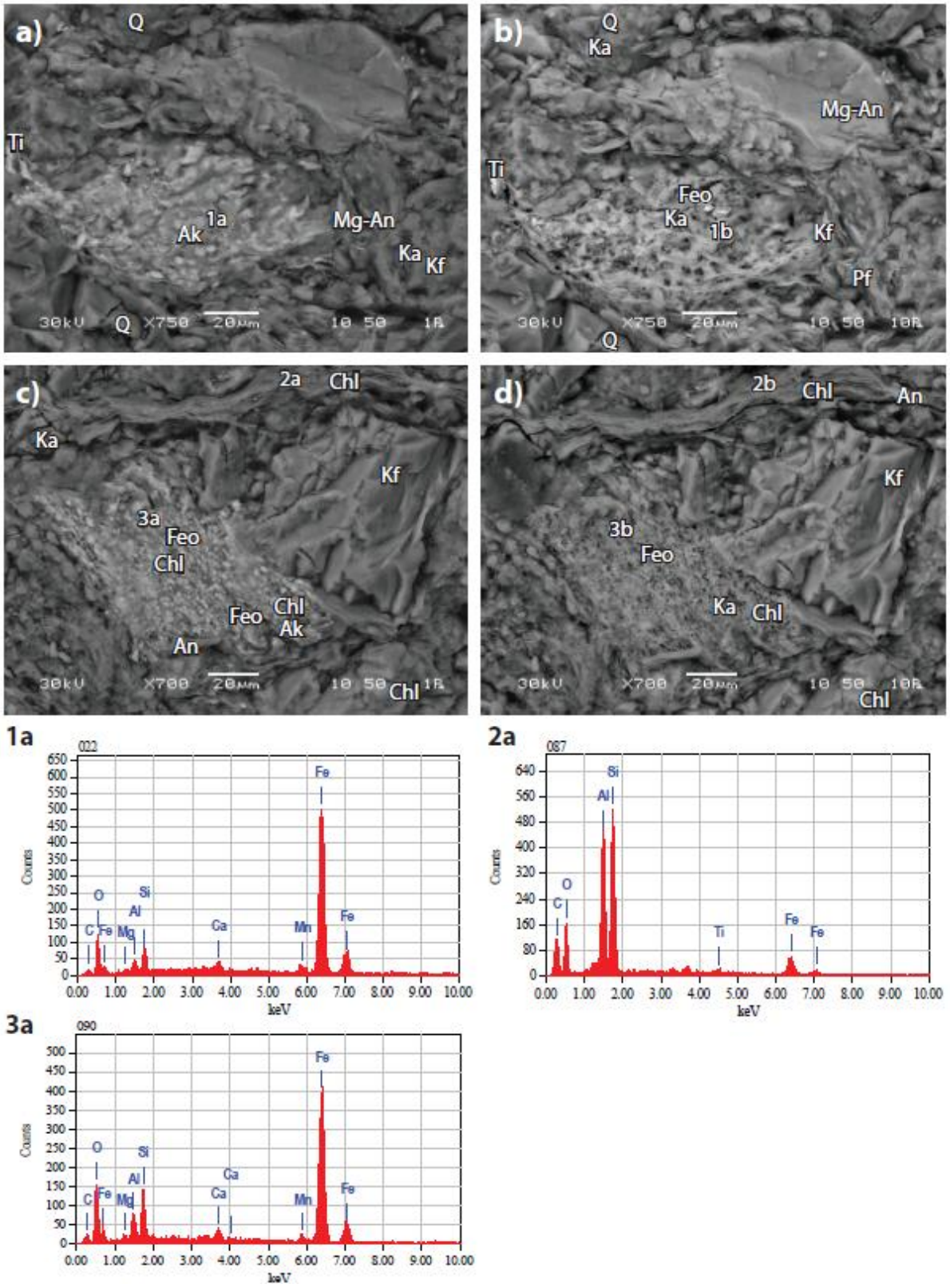
a)
Q
Ti
Ak
1a
Mg-An
Ka
Kf
30kU Q X750 20µm 10 50 1R
b)
Q
Ka
Mg-An
Ti
Feo
Ka
1b
Kf
Pf
Q
30kU X750 20µm 10 50 10R
c)
2a
Chl
Ka
Kf
3a
Feo
Chl
Feo
Chl
Ak
An
30kU X700 20µm 10 50 Chl 1R
d)
2b
Chl
An
Kf
3b
Feo
Ka
Chl
30kU X700 20µm 10 50 10R
Chl
1a
022
Fe
O
Si
Al
C
Fe
Mg
Ca
Mn
Fe
Counts
keV
2a
087
Si
Al
O
C
Ti
Fe
Fe
Counts
keV
3a
090
Fe
O
Si
Al
Ca
C
Fe
Mg
Ca
Mn
Fe
Counts
keV

Figure 12

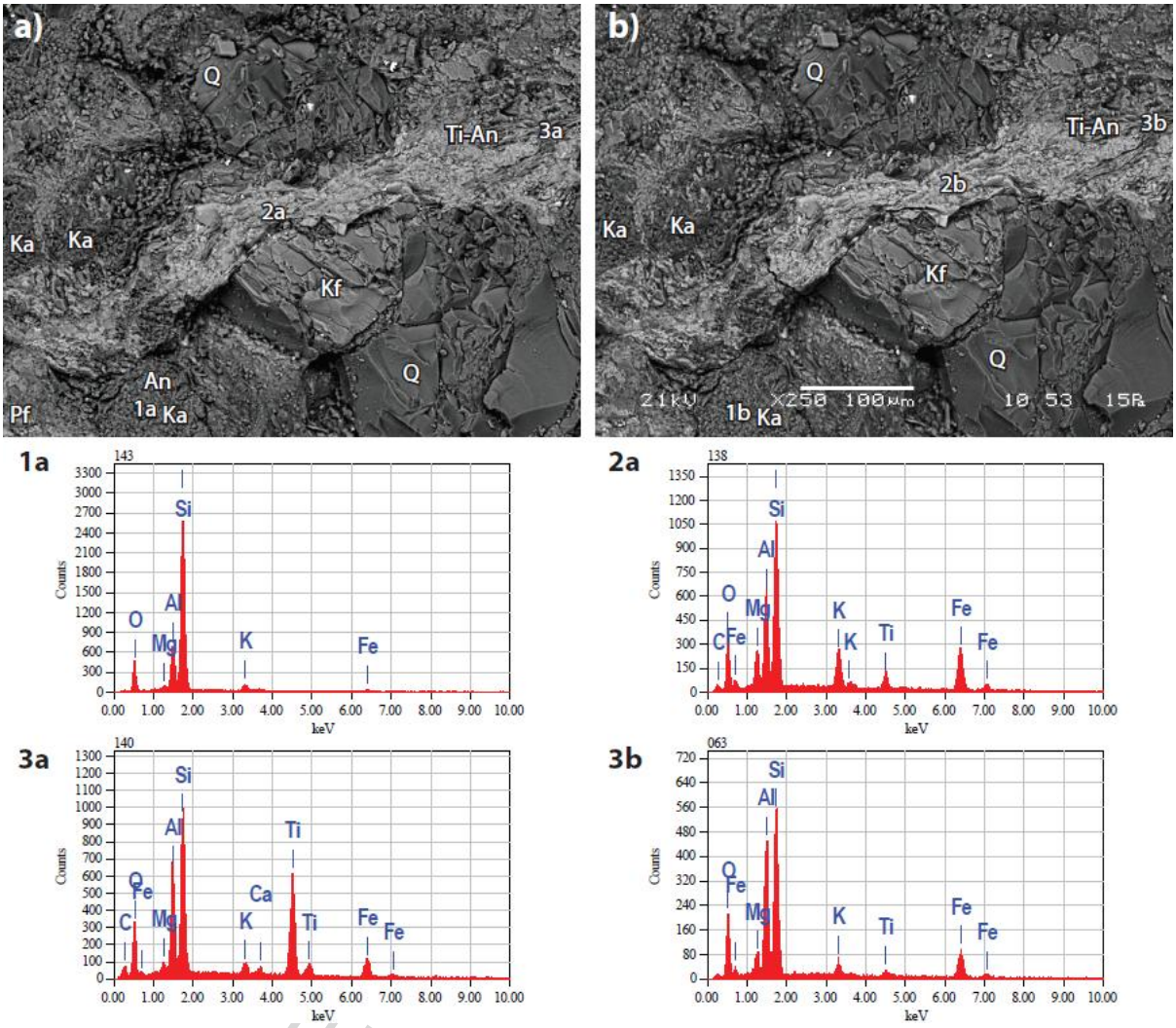

Figure 13

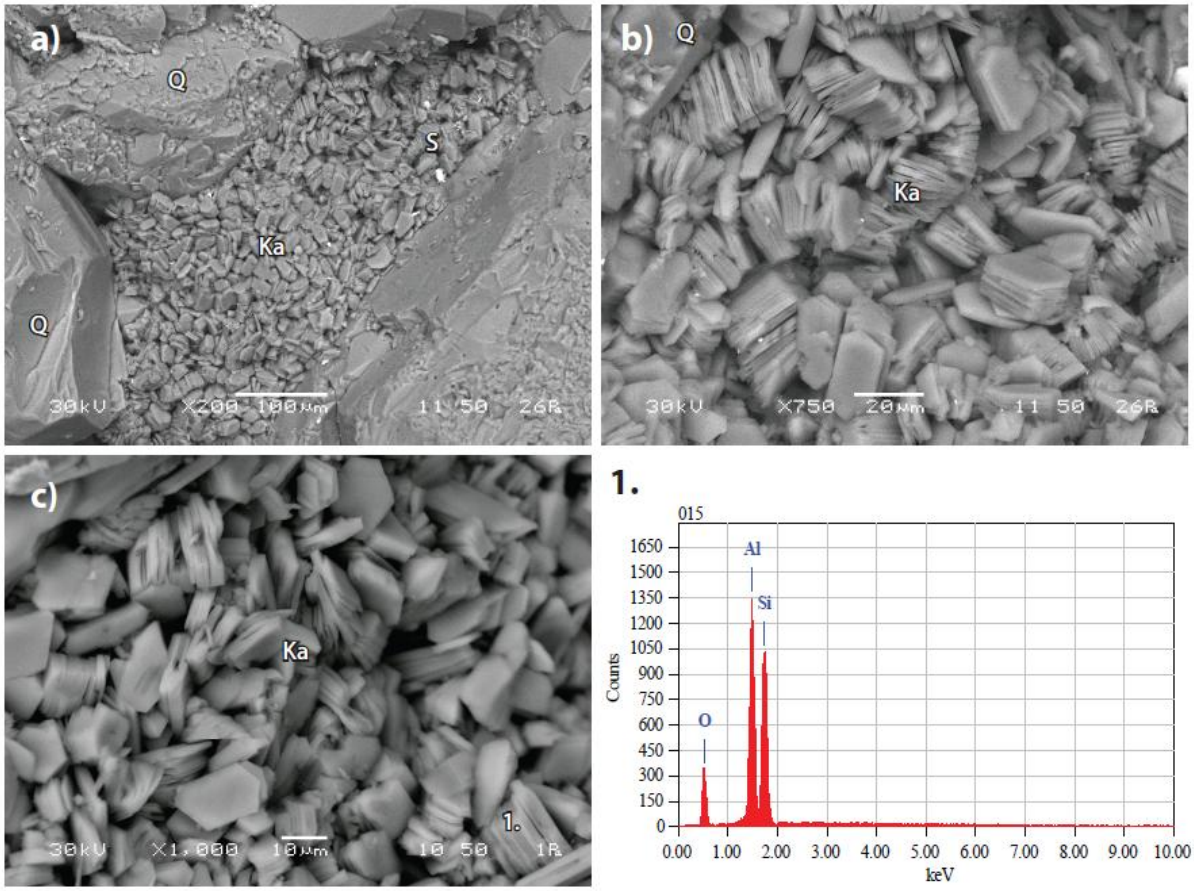

Figure 14

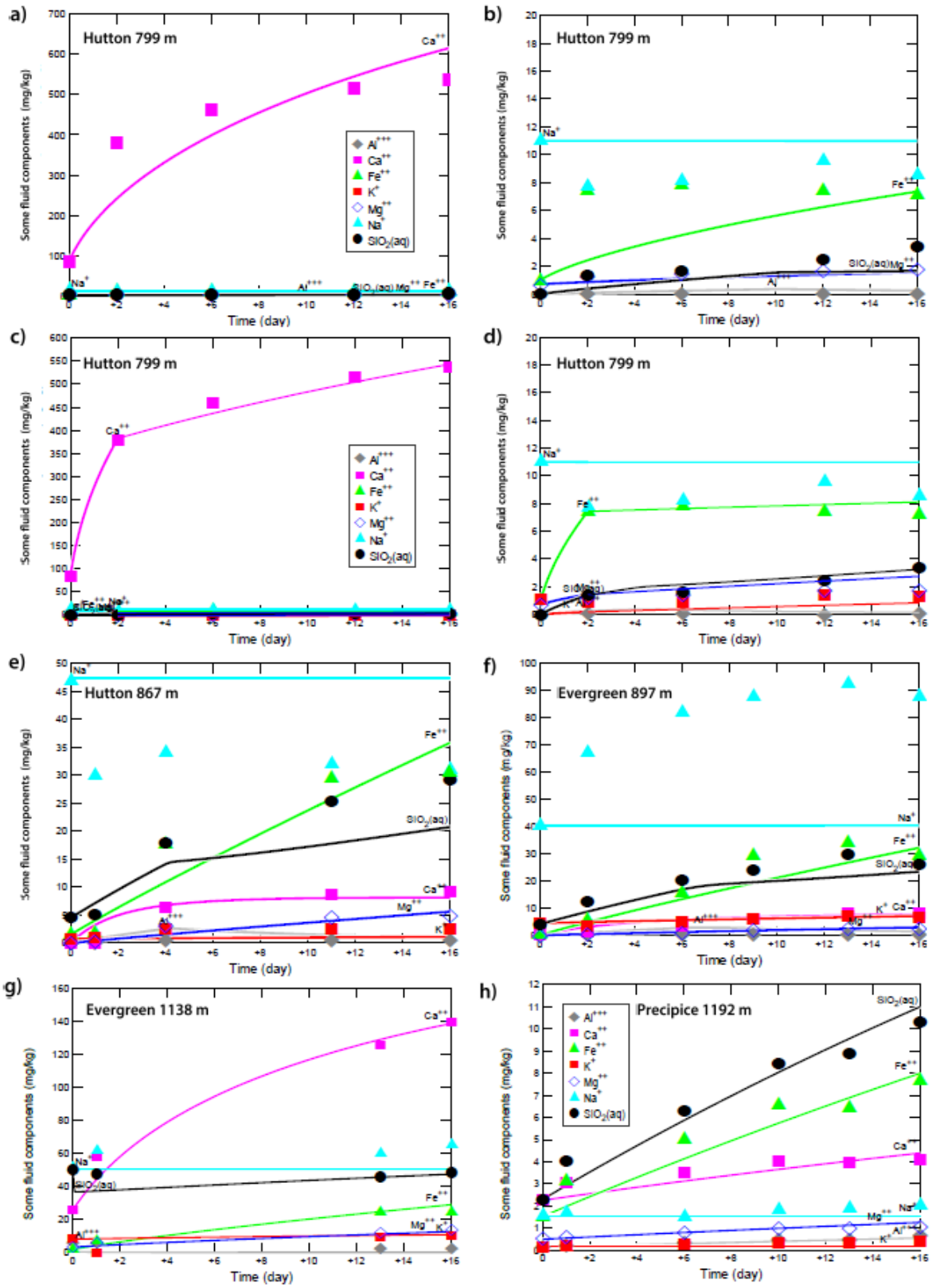
a)
Hutton 799 m
Some fluid components (mg/kg)
Time (day)
Al+++
Ca++
Fe++
K+
Mg++
Na+
SiO2(aq)
b)
Hutton 799 m
c)
Hutton 799 m
d)
Hutton 799 m
e)
Hutton 867 m
f)
Evergreen 897 m
g)
Evergreen 1138 m
h)
Precipice 1192 m

Figure 15

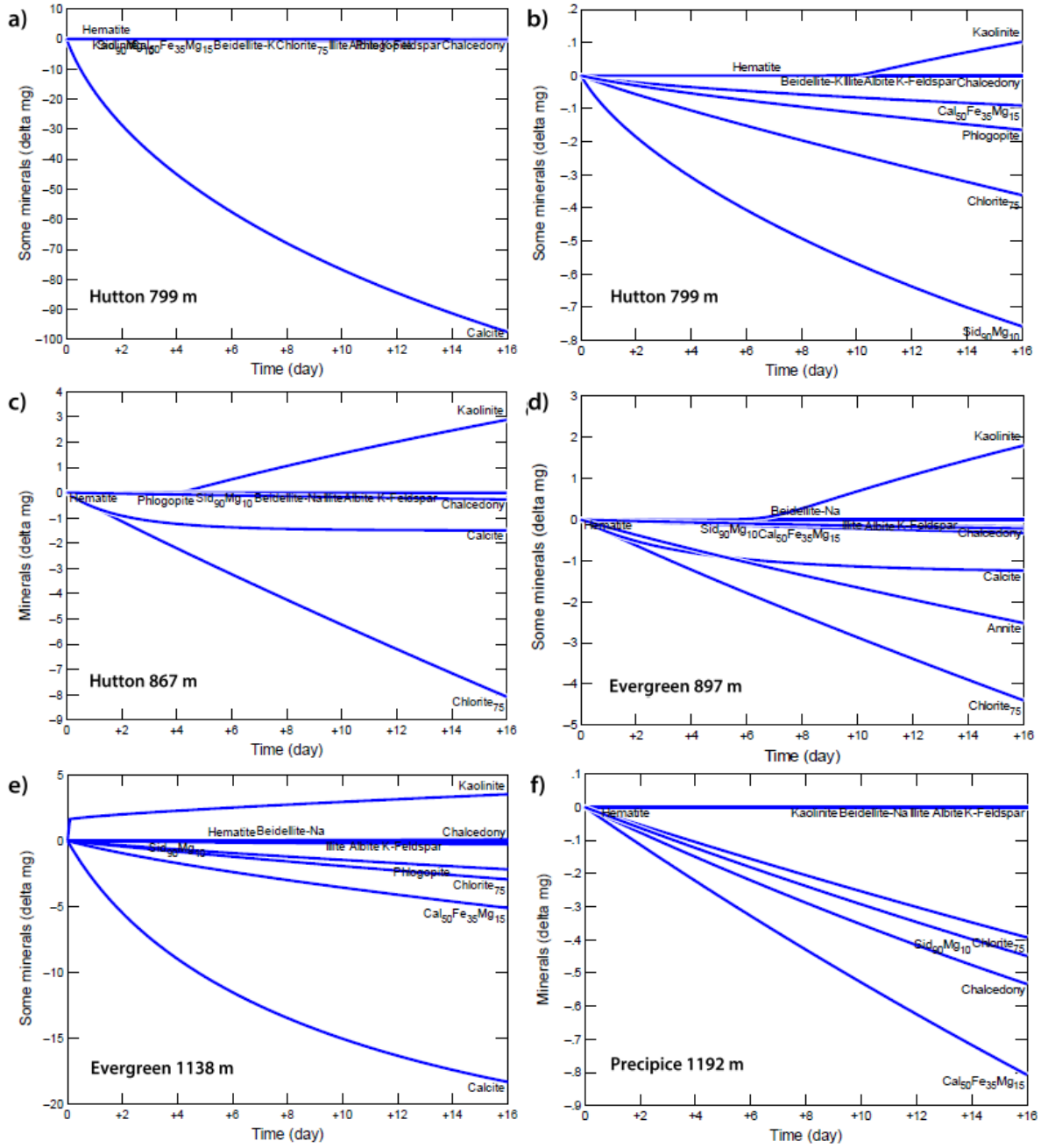

Figure 16

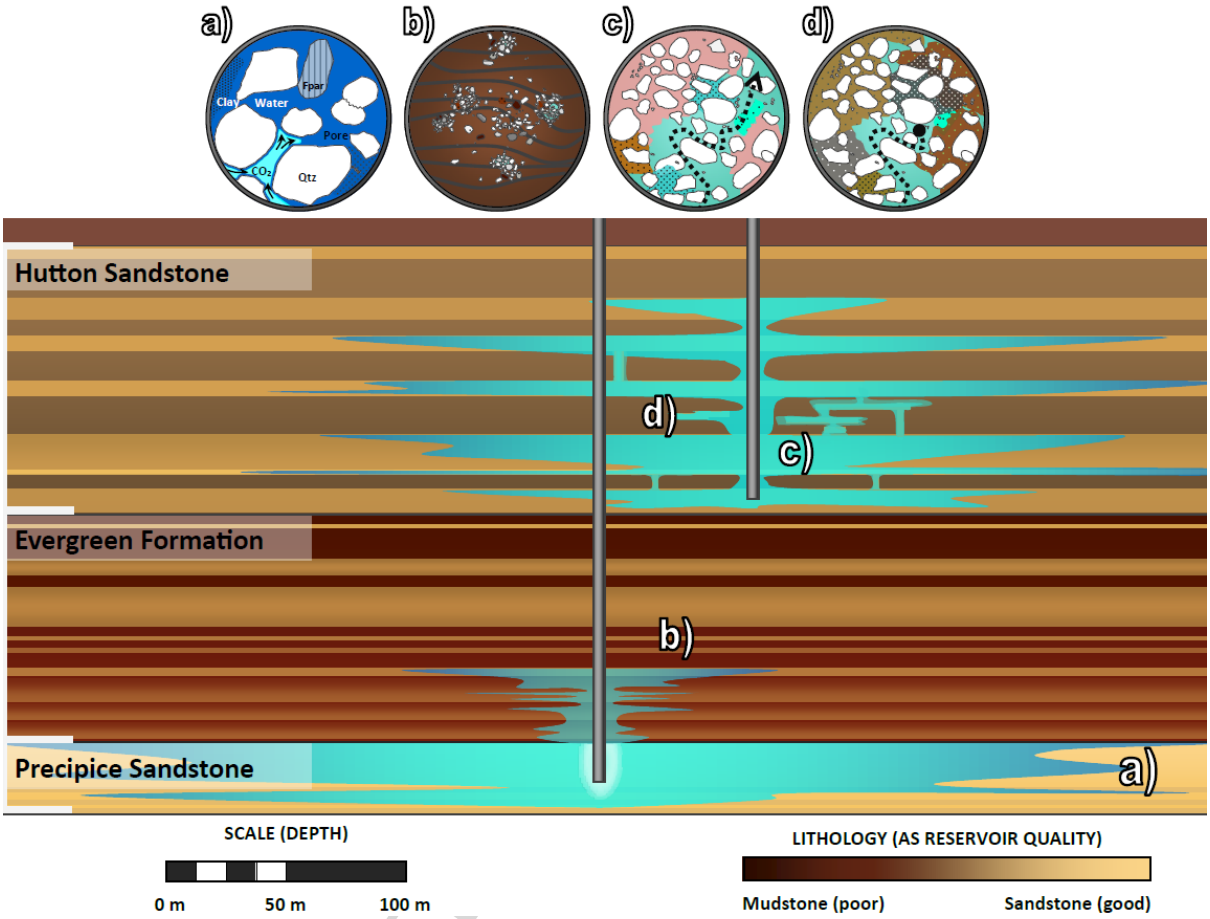

Figure 17

Table 1:

Experiment stage	Fluid-gas phase	Pressure (bar)	Temperature (°C)	Effluent samples	Rock added	Stage length (days)
CO_2-clean	$CO_2 + H_2O$	120 ± 1	60 ± 0.5	0	No	2–5
CO_2-blank	$CO_2 + H_2O$	120 ± 1	60 ± 0.5	1	No	1–2
N_2-baseline	$N_2 + H_2O$	120 ± 1	60 ± 0.5	1	Yes	1–2
CO_2-reaction	$CO_2 + H_2O$	120 ± 1	60 ± 0.5	3–5	Yes	~16

Table 2:

Sample	Mass (g)			Approx. dimensions (mm)	
	A cube	A offcut	B half-cube	A plug diameter	A plug length
Hutton 799 m	5.9204	3.0395	2.2725	4	7
Hutton 867 m	5.5312	3.0343	4.2223	3	5
Evergreen 897 m	5.2504	2.822	3.0925	3	5
Evergreen 1138 m	5.3018*	2.4512*	3.068	3	5
Precipice 1129 m	5.6473	2.749	2.621	8	8

* Experiment conducted in 1 % KCl solution for run A to preserve sample integrity, and purified water for Run B to identify geochemical trends in experiment fluids.

Table 3:

Mineral	$K_{25(acid)}$ (mol/cm2/s)	$E_{a(acid)}$ (kJ/mol)	n	$K_{25(neut)}$ (mol/cm^2/s)	$E_{a(neut)}$ (kJ/mol)	A_s^* (cm^2/g)	$K_{(precip)}$ (mol/cm^2/s)	Γ
Quartz				1.70E-17	68.7	1.E+04	$K_{(diss)}$	2.E+10
K-feldspar	8.71E-15	51.7	0.5	3.89E-17	38	10	$K_{(diss)}$	2.E+10
Albite	6.92E-15	65	0.457	2.75E-17	69.8	10	$K_{(diss)}$	2.E+10
Kaolinite	4.90E-16	65.9	0.777	6.61E-18	22.2	10	$K_{(diss)}$/10	2.E+10
Illite / muscovite	1.91E-16	46	0.6	8.91E-20	14	70	$K_{(diss)}$	2.E+10
Smectite	1.05E-15	23.6	0.34	1.66E-17	35	150	$K_{(diss)}$	2.E+10
Biotite	1.45E-14	22	0.525	2.82E-17	22	15	$K_{(diss)}$	2.E+10
Fe-chlorite	1.62E-14	25.1	0.49	1.00E-17	94.3	7000	$K_{(diss)}$	2.E+10
Calcite	5.01E-05	14.4	1	1.55E-10	23.5	10	$K_{(diss)}$	1.E+10
Ankerite	1.59E-08	45	0.9	1.26E-13	62.76	10	$K_{(diss)}$/1e5	3.E+10
Siderite	1.59E-08	45	0.9	1.26E-13	62.76	10	$K_{(diss)}$	2.E+10
Fe-oxide	4.07E-14	66.2	1	2.51E-19	66.2	10	$K_{(diss)}$	1.E+10

*initial surface areas.

Table 4:

Oxide (wt%)	Precipice 1192 m	Evergreen 1138 m	Evergreen 897 m	Hutton 867 m	Hutton 799 m	Maximum 2σ uncertainty
SiO_2	97.9	74.1	66.3	80.2	81.9	4.8
TiO_2	0.1	0.6	0.9	0.6	0.1	0.02
Al_2O_3	1.8	15.1	16.6	10.2	2.3	0.8
Fe_2O_3	0.1	2.7	3.4	3.9	0.5	0.2

MnO	0.00	0.03	0.05	0.03	0.34	0.05
MgO	0.00	0.76	0.72	0.43	0.04	0.03
CaO	0.0	1.0	0.2	0.1	10	0.2
Total Ca	0.0	0.7	0.1	0.0	7.0	
Na_2O	0.1	1.3	1.7	0.8	0.3	0.7
K_2O	0.0	2.8	2.6	1.1	0.3	1.1
P_2O_5	0.02	0.11	0.07	0.06	0.03	0.01
LOI	0.8	3.1 ± 2.5*	7.2	3.2	8.4	
Total	100.8	100.7	99.8	100.5	104.0	

*Theoretical LOI calculated from total major oxides, with associated calculation error.

Table 5:

Component	Precipice Sandstone 1192 m	Evergreen Formation 1138 m	Evergreen Formation 897 m	Hutton Sandstone 867 m	Hutton Sandstone 799 m
Grain components					
Framework grains	78.0	34.4	18.9	59.4	76.3
Matrix material	–	60.4	77.2	–	–
Clay, mica, weathered feldspar content	7.7	–	–	35.8	5.6
Calcite cement	–	–	–	–	17.0
Heavy minerals	0.2	4.9	1.9	2.9	<0.1
Porosity components					
Resolved porosity	18.0	–	–	1.9	1.1
Resolvable porosity ± organic content*	–	0.2	2.0	–	–

*Resolvable porosity, including possible organic content. Resolved porosity indicates pores larger than 1 voxel (3D pixel) in size.

Table 6:

Mineral	Precipice Sandstone 1192 m	Evergreen Formation 1138 m	Evergreen Formation 897 m	Hutton Sandstone 867 m	Hutton Sandstone 799 m
Quartz	97.8	35.7	39.7	56.6	78.1
Alkali Feldspar	<0.1	26.5	5.7	7.2	1.1
Plagioclase	<0.1	7.8	9.3	6.4	2.2
Muscovite/Illite	<0.1	1.8	10.0	6.0	0.2
Biotite	0.0	0.4	1.1	0.5	<0.1
Kaolinite	1.3	12.4	19.2	6.9	2.5
Chlorite	<0.1	3.1	3.8	8.3	0.3
Glauconite	0.0	<0.1	0.1	0.2	<0.1
Smectite	0.0	0.4	<0.1	0.0	0.0
Calcite	0.0	0.2	0.0	0.0	14.6
Siderite	0.0	0.0	<0.1	<0.1	0.0
Apatite	0.0	<0.1	<0.1	<0.1	0.0

Rutile	0.0	<0.1	0.2	0.2	0.0
Pyrite	0.0	<0.1	0.0	0.0	0.0
Fe-Oxides	0.0	0.0	0.2	0.1	0.0
Zircon	<0.1	<0.1	<0.1	0.0	0.0
Unresolvable material + ∑trace minerals	0.8	11.4	10.6	7.6	1.0
Resolved porosity	18.4	0.2*	2.0*	1.9	1.1

*Resolvable porosity with possible organic content

Table 7:

	Composition (%)										
Mineral	Na_2O	CaO	K_2O	Al_2O_3	SiO_2	FeO	MnO	MgO	SrO	TiO_2	Total
Hutton Sandstone 799 m											
Calcite		58.4	0.02			0.02	0.86	1.61	0.12	0.12	61.1
Kaolin	0.01	0.14	0.04	32.8	40.2			0.01	0.01		73.2
Orthoclase	1.04		15.6	17.2	60.8	0.02					94.7
Quartz	0.00	0.38	0.00	0.02	95.4				0.02	0.01	95.8
Chlorite	0.16	0.10	0.55	18.9	25.8	33.4	0.31	4.05	0.19	0.63	84.1
Illite	0.67	0.02	5.75	17.9	50.3	11.8	0.04	1.82	0.27	0.24	88.8
Hutton Sandstone 867 m											
Kaolin	0.12	0.16	0.03	37.9	45.5	0.14		0.03	0.03		84.0
Muscovite	0.46		9.31	30.5	42.2	3.59	0.03	0.69		0.57	87.4
Orthoclase	0.67		15.9	17.8	64.6	0.13	0.01			0.01	99.1
Quartz		0.41		0.01	102	0.02	0.02		0.01	0.01	102
Ilmenite	0.01			0.08	0.17	33.0	0.73	0.59	0.15	54.7	89.4
Evergreen Formation 897 m											
Quartz		0.35	0.01		99.8	0.02			0.01	0.02	100
Illite	0.13		6.73	28.7	51.2	3.09	0.04	2.44	0.07	0.10	92.5
Kaolin	0.14	0.20	0.12	36.9	49.1	2.24	0.02	0.35	0.16	0.02	89.3
Orthoclase	0.61		16.3	18.6	65.7	0.02	0.02			0.02	101
Quartz	0.08	0.20	0.43	3.33	88.4	1.07					93.5
*Evergreen Formation 1138 m**											
Chlorite	0.42	0.06	1.34	20.6	30.2	20.8	0.12	5.73	3.94	0.10	83.3
Muscovite	1.61	0.00	10.4	25.9	42.9	0.60		0.22	0.18	0.49	82.3
Orthoclase	0.03		13.6	15.3	57.1	0.02				0.01	86.1
Quartz		0.35	0.01	0.05	98.3			0.01	0.01	0.02	98.7
Chlorite	2.20	0.12	0.06	33.1	33.7	14.0	0.19	0.65	0.22	0.31	84.5
Precipice Sandstone 1192 m											
Kaolin	0.12	0.13	0.04	36.3	45.5	0.13	0.01	0.10	1.59		83.9
Quartz	0.01	0.37		0.01	101						101

*Carbonate also identified.

Table 8:

	Precipice Ss 1192 m	Evergreen Fm 1138 m	Evergreen Fm 898 m	Hutton Ss 868 m	Hutton Ss 799 m
Sample mass (m)					
m pre-CO_2 (g)	3.012	3.068	2.819	4.222	2.273
m post-CO_2 (g)	3.004	2.994	2.753	4.200	2.184
Δm after CO_2 reaction (g)	-0.009	-0.07	-0.07	-0.02	-0.09
Helium density (pHe)					
pHe pre-CO_2 (g/cm^3)	2.667 (0.005)	2.583 (0.004)	2.543 (0.008)	2.81 (0.01)	2.700 (0.006)
pHe post-CO_2 (g/cm^3)	2.611 (0.003)	2.597 (0.007)	2.573 (0.008)	2.649 (0.004)	2.624 (0.009)
Δ pHe after CO_2 reaction (g/cm^3)	-0.06	0.01	0.03	-0.17	-0.08
Apparent skeletal (mercury) density (ρHg)					
ρHg pre-CO_2	2.61	2.54	2.58	2.10	2.30
ρHg post-CO_2	2.78	2.62	2.57	2.27	2.10
$\Delta\rho$Hg after CO_2 reaction (cm^3)	0.2	0.1	0.0	0.2	-0.2
Mercury porosity (Φ)					
Φ pre-CO_2 (%)	15.2	8.8	6.1	7.9	10.1
Φ post-CO_2 (%)	14.9	9.3	6.8	11.9	8.4
$\Delta\Phi$ after CO_2 reaction (cm^3)	-0.4	0.6	0.7	4.0	-1.7

*Standard deviations shown in parentheses.

Table 9:

Mineral	Precipice 1192 m		Evergreen 1138 m		Evergreen 897 m		Hutton 867 m		Hutton 799 m	
	Before	After	Before	After	Before	After	Before	After	Before	After
Quartz	97.8	98.0	35.7	45.2	39.7	39.8	56.6	58.9	78.1	74.2
Alkali Feldspar	<0.1	0.0	26.5	20.8	5.7	6.4	7.2	6.3	1.1	3.1
Plagioclase	<0.1	<0.1	7.8	5.6	9.3	8.4	6.4	6.4	2.2	1.6
Muscovite/Illite	<0.1	0.4	1.8	1.1	10.0	10.6	6.0	2.9	0.2	0.2
Biotite	0.0	0.0	0.4	0.5	1.1	1.8	0.5	0.3	<0.1	<0.1
Kaolinite	1.3	1.4	12.4	10.5	19.2	20.4	6.9	10.7	2.5	3.6
Chlorite	<0.1	<0.1	3.1	3.3	3.8	3.2	8.3	8.5	0.3	0.2
Glauconite	0.0	0.0	<0.1	0.1	0.1	0.2	0.2	<0.1	<0.1	<0.1
Smectite	0.0	0.0	0.4	<0.1	<0.1	<0.1	0.0	<0.1	0.0	0.0
Calcite	0.0	0.0	0.2	0.0	0.0	0.0	0.0	<0.1	14.6	13.2
Siderite	0.0	0.0	0.0	0.0	<0.1	0.0	<0.1	0.0	0.0	0.0
Apatite	0.0	0.0	<0.1	<0.1	<0.1	<0.1	<0.1	<0.1	0.0	0.0
Rutile	0.0	0.0	<0.1	<0.1	0.2	0.1	0.2	<0.1	0.0	<0.1
Pyrite	0.0	0.0	<0.1	0.0	0.0	0.0	0.0	0.0	0.0	0.0
Fe-Oxides	0.0	0.0	0.0	0.0	0.2	0.2	0.1	<0.1	0.0	0.0
Zircon	<0.1	0.0	<0.1	0.0	<0.1	<0.1	0.0	0.0	0.0	0.0
Unclassified material + ∑Trace minerals	0.8	0.2	11.4	12.8	10.6	9.0	7.6	5.9	1.0	3.8

Table 10:

Component	Precipice Sandstone 1192 m		Evergreen Formation 1138 m		Evergreen Formation 897 m		Hutton Sandstone 867 m		Hutton Sandstone 799 m	
	Pre-CO_2	Post-CO_2	Pre-CO_2	Post-CO_2	Pre-CO_2	Post-CO_2	Pre-CO_2	Post-CO_2	Pre-CO_2	Post-CO_2
Mineral components										
Framework grains	78.0	77.4	34.4	31.8	18.9	17.5	59.4	60.6	76.3	75.9
Matrix and/or framework grains*	–	–	60.4	63.1	77.2	77.9	–	–	–	–
Clays / micas / ex-feldspars	7.7	7.9	–	–	–	–	35.8	33.8	5.6	6.9
Calcite cement	–	–	–	–	–	–	–	–	17.0	14.9
Heavy minerals	0.2	0.2	4.9	4.1	1.9	2.8	3.0	3.9	<0.1	<0.1
Porosity components										
Resolvable porosity	18.0	18.4	–	–	–	–	1.9	1.7	1.1	2.2
Resolved porosity / organic*	–	–	0.2	1.0	2.0	1.7	–	–	–	–

*Porosity in the two Evergreen Formation samples contains substantial pore-filling material, with resolvable pores limited to those >1 voxel (3D pixel) in size; complex, fine-grained lithology does not allow sub-resolution pores to be distinguished from more x-ray "dense" material.

Table 11:

	Precipice Sandstone 1192.9 m	Evergreen Formation 1138 m	Evergreen Formation 897.9 m	Hutton Sandstone 867 m	Hutton Sandstone 799.5m
Quartz	94.5	43.5	50.0	62.0	78.0
K-Feldspar	0.8	16.2	8.5	8.5	3.2
Plagioclase Feldspar	0.2	12.3	15.5	6.5	2.1
Kaolin	2.1	3.7	10.4	6.5	2.0
Illite / muscovite	1.0	4.0	5.0	2.5	0.2
Smectite (Na-rich)	0.3	6.5	1.3	0.9	0.1
Biotite (Fe- or Fe,Mg-)	0.0	4.6	4.0	0.5	0.2
Fe-Chlorite (Fe_3:Mg_1)	0.2	2.5	2.5	8.5	0.3
Calcite	0.0	1.1	0.1	0.1	13.5
Ankerite ($Ca_1Fe_{0.7}Mg_{0.3}$)	0.5	3.8	0.1	0.0	0.1
Siderite ($Fe_{0.9}Mg_{0.1}$)	0.5	1.9	0.6	0.1	0.3
Fe-oxides	0.1	0.1	2.0	4.0	0.2

Highlights:

- CO_2 batch-reaction experiments were conducted at simulated storage conditions
- Whole-rock samples of varied mineralogy from a low-salinity reservoir were examined
- Detailed sample characterisation was conducted pre- and post-CO_2 to note changes
- Experiments were coupled with micro-computed tomography and kinetic modelling
- Fluid chemistry and petrography reveal dissolution of carbonates and some silicates